SANDIA REPORT
SAND2009-6396
Unlimited Release
Printed October 2009

Resolving Dynamics of Cell Signaling via Real-Time Imaging of the Immunological Synapse

Jerilyn A. Timlin, Jesse S. Aaron, Amanda Carroll-Portillo, Bryan D. Carson, Janet R. Pfeiffer, Keith A. Lidke, Kathrin Spendier, Roberto Rebeil, Dina T. Mirijanian, Mark A. Stevens, James L. Thomas, Janet M. Oliver, Bridget S. Wilson, Alan R. Burns

Prepared by
Sandia National Laboratories
Albuquerque, New Mexico 87185 and Livermore, California 94550

Sandia is a multiprogram laboratory operated by Sandia Corporation,
a Lockheed Martin Company, for the United States Department of Energy's
National Nuclear Security Administration under Contract DE-AC04-94AL85000.

Approved for public release; further dissemination unlimited.

Issued by Sandia National Laboratories, operated for the United States Department of Energy by Sandia Corporation.

NOTICE: This report was prepared as an account of work sponsored by an agency of the United States Government. Neither the United States Government, nor any agency thereof, nor any of their employees, nor any of their contractors, subcontractors, or their employees, make any warranty, express or implied, or assume any legal liability or responsibility for the accuracy, completeness, or usefulness of any information, apparatus, product, or process disclosed, or represent that its use would not infringe privately owned rights. Reference herein to any specific commercial product, process, or service by trade name, trademark, manufacturer, or otherwise, does not necessarily constitute or imply its endorsement, recommendation, or favoring by the United States Government, any agency thereof, or any of their contractors or subcontractors. The views and opinions expressed herein do not necessarily state or reflect those of the United States Government, any agency thereof, or any of their contractors.

Printed in the United States of America. This report has been reproduced directly from the best available copy.

Available to DOE and DOE contractors from
U.S. Department of Energy
Office of Scientific and Technical Information
P.O. Box 62
Oak Ridge, TN 37831

Telephone: (865) 576-8401
Facsimile: (865) 576-5728
E-Mail: reports@adonis.osti.gov
Online ordering: http://www.osti.gov/bridge

Available to the public from
U.S. Department of Commerce
National Technical Information Service
5285 Port Royal Rd.
Springfield, VA 22161

Telephone: (800) 553-6847
Facsimile: (703) 605-6900
E-Mail: orders@ntis.fedworld.gov
Online order: http://www.ntis.gov/help/ordermethods.asp?loc=7-4-0#online

SAND2009-6396
Unlimited Release
Printed October 2009

Resolving Dynamics of Cell Signaling via Real-Time Imaging of the Immunological Synapse

Jerilyn A. Timlin, Jesse S. Aaron, Bryan D. Carson, Roberto Rebeil[†]
Biofuels and Defense Technologies

Dina T. Mirijanian[‡], Mark A. Stevens
Computational Materials Science and Engineering

Alan R. Burns
ST&E Strategy and University Research

Sandia National Laboratories
P.O. Box 5800
Albuquerque, New Mexico 87185-0895

Amanda Carroll-Portillo[§], Janet R. Pfeiffer, Janet M. Oliver, Bridget S. Wilson
Department of Pathology and Cancer Research and Treatment Center

Keith A. Lidke[§], Kathrin Spendier, James L. Thomas
Department of Physics and Astronomy

University of New Mexico,
Albuquerque, New Mexico 87131

Abstract

This highly interdisciplinary team has developed dual-color, total internal reflection microscopy (TIRF-M) methods that enable us to optically detect and track in real time protein migration and clustering at membrane interfaces. By coupling TIRF-M with advanced analysis techniques (image correlation spectroscopy, single particle tracking) we have captured subtle changes in membrane organization that characterize immune responses. We have used this approach to elucidate the initial stages of cell activation in the IgE signaling network of mast cells and the Toll-like receptor (TLR-4) response in macrophages stimulated by bacteria. To help interpret these measurements, we have undertaken a computational modeling effort to connect the protein motion and lipid interactions. This work provides a deeper understanding of the initial stages of cellular response to external agents, including dynamics of interaction of key components in the signaling network at the "immunological synapse," the contact region of the cell and its adversary.

[†] Current address: National Biodefense Analysis and Countermeasures Center, Frederick, MD
[‡] Current address: Theory of Nanostructured Materials Facility, Molecular Foundry, Lawrence Berkeley National Laboratory, Berkeley, CA 94720
[§] ACP and KAL also made significant contributions to this work while postdoctoral researchers at Sandia National Laboratories, Albuquerque, NM

ACKNOWLEDGMENTS

The authors wish to acknowledge the following people for their contributions to this project (in alphabetical order):

- George Bachand (Sandia National Laboratories): *Project management and kind loan of microinjection device*
- Kevin Crown (Sandia National Laboratories): *liposome characterization*
- Ryan Davis (Sandia National Laboratories): *hyperspectral imaging of immune cells*
- Adrienne Greene (Sandia National Laboratories), Sheli Ryan, and Marina Martinez (UNM Department of Pathology): *assistance with cell culture, reagent labeling, and biochemical assays throughout this project*
- Gary Griffiths, Haitao Li, Shannon Cofiell, and Nalini Shenoy (NIH Imaging Probe Development Center): *synthesis of fluorescent cholesterol analogs*
- Gabriel Montano (Center for Integrated NanoTechnologies): *supported lipid bilayer methods*

CONTENTS

1. Introduction 11

2. Development of Imaging and Analysis Capabilities 13
   2.1 Total Internal Reflectance Fluorescence (TIRF) Instrumentation 13
      2.1.1 TIRF Principles 13
      2.1.2 Instrumentation 14
   2.2 Image Analysis Software 16
      2.2.1 Automated Image Alignment and Calibration 16
      2.2.2 Quantitative Image Analysis 17

3. Imaging IgE Immune Response in Mast Cells 19
   3.1 The Actin Cytoskeleton and FcεRI Dynamics 19
   3.2 The Mast Cell Synapse 19
      3.2.1 Formation of Synaptic Regions 20
      3.2.2 Mast Cell Signaling Through the Synapse 21
      3.2.3 Cholesterol and the Mast Cell Synapse 22
      3.2.4 Synapse Formation Delineation by the Actin Cytoskeleton 25
      3.2.5 Synopsis 26
   3.3 Mechanism of FcεRI Receptor Cluster Formation 26
      3.3.1 Pipette Manipulation of Cells 27
      3.3.2 Image Correlation Spectroscopy with Explicit Noise Removal 27
      3.3.3 Initial Receptor Clusters Form at Cell Protrusions by Diffusion-Mediated Trapping 28
   3.4 Development of a Single-Cell Degranulation Assay 30
      3.4.1 Model system for Visualization of Degranulation 30
      3.4.2 FasL:GFP Dynamics During Cell Stimulation 31
      3.4.3 Quantifying Degranulation at the Single Cell Level 32

4. Imaging of TLR-4 Receptor Response to Bacterial Antigens 35
   4.1. The Role of TLR4 in Innate Immunity 35
   4.2 LPS Can Be Modified to Subvert Detection 35
   4.3 Purification, Testing, and Labeling of LPS 36
   4.4 Simultaneous TIRF Imaging of LPS and TLR4 in Live Cells 37

5. Molecular Dynamics of Proteins in Lipid Bilayer 41

6. Conclusions 43

4. References 45

Appendix A: Summary of Presentations and Publications 47

Distribution 49

FIGURES

Figure 1: TIRF concept. A laser light source is directed at an oblique angle, and refracted through a glass substrate. At incident angles greater than the critical angle, light is totally internally reflected, producing a narrow evanescent field that illuminates only the first *ca.* 100nm of the sample above the glass. This geometry is ideal for investigations involving interfacial phenomena, such as ligand-membrane receptor binding in cells. The overall penetration depth of the evanescent field is a function of both the illumination wavelength and the incident angle. .. 14

Figure 2: Optical setup of our multi-color TIRF microscope. Up to two different wavelengths can be introduced onto the sample simultaneously. The high-NA TIRF objective focuses the lasers at an oblique angle, thus producing the total internal reflectance condition. Emitted fluorescence (red and green-blue lines) can be spectrally separated using the Optosplit image splitter (Cairns Research), and projected onto spatially distinct regions of the EMCCD camera (Andor)..... 16

Figure 3: TIRF images of IgE^{DNP} primed cells after 12 minutes upon a 5, 10, and 25 mol% DNP-DPPE containing bilayer..... 20

Figure 4: Degranulation assay to measure β-Hexosaminidase release from IgE^{DNP}-primed RBL-2H3 cells stimulated with mobile and immobilized ligand. Release is measured as percent total of lysate samples. Bilayers presenting 10 mol% and 25 mol% as well as soluble and immobilized DNP-BSA resulted in significant levels of degranulation above the background (spontaneous release from cells contacting glass without antigen). 21

Figure 5: Fluorescent recovery within synaptic region after photobleaching. Box with dashed line represents portion of field of view photobleached. Images in the right column are the photobleached are immediate, 6 minutes, and 8 minutes post-bleach. Grayscale indicator is level of intensity within each image. 22

Figure 6: TIRF and TEM images of localization of cholesterol within the contacting membrane. IgE^{DNP} primed cells repleted with FITC (left image, upper row) or NBD-6 (middle image, upper row) fluorescent cholesterol and settled on 25 mol% DNP-DPPE bilayers. FITC cholesterol repleted cells primed with IgE^{DNP} were also settled onto immobilized DNP-BSA (right image, upper row). Membrane sheets from FITC-cholesterol repleted, IgE^{DNP} primed cells on either 25 mol% DNP-DPPE bilayers (left image, lower row) or immobilized DNP-BSA stained for FcεRI (12 nm) and FITC (6 nm). On sheets from mobile ligand substrate, regions containing both receptor and cholesterol are outlined. On sheets from immobilized DNP-BSA surfaces, cholesterol label is highlighted with receptor label circled in the surrounding membrane region. 24

Figure 7: Localization of LAT relative to receptor in membrane sheets isolated from 25 mol% DNP-DPPE bilayers (upper image) or immobilized DNP-BSA (bottom image) surfaces. Receptors (12 nm gold) are circled with dashed lines while LAT (6 nm gold) clusters are circled with solid lines. 25

Figure 8: TIRF image of actin-GFP IgE^{DNP} primed RBL-2H3 cell settling onto a 25 mol% DNP-DPPE bilayer. Actin is green and receptors are red..... 26

Figure 9: Top Row. TIRF images of DY520-XL-labeled IgE in receptor clusters, on a RBL-2H3 cell in contact after approximately (A) 45 seconds and (B) 5 minutes with a POPC bilayer with

10 mol% ligand lipids. Cell settled due to gravity. Bottom Row. (C) TIRF image of Alexa488-labeled IgE on a RBL-2H3 cell at initial contact with a POPC bilayer with 25 mol% ligand lipids. This cell was pushed down with a micropipette. (D) a micrograph showing a RBL-2H3 cell held approximately 1 μm above the surface with a micropipette. Bar = 5 μm..... 27

Figure 10: Image correlation was performed to determine the size of heterogeneity and g(0) of single cells pipette-pressed against a stimulating surface. Rotationally averaged correlation showing explicit noise removal and half width of receptor clusters. Inset (A) is TIRF image of RBL cell and (B) is same image masked with mean of cell interior analyzed here. Bar = 5 μm. 28

Figure 11: Size of IgE receptor heterogeneities on different surfaces within five seconds of contact. The spatial scale of heterogeneities is the same for crosslinked DNP-BSA and their control surfaces which suggests that the mechanism of IgE receptor aggregation is trapping at cell protrusions. The error bars represent the standard deviation from multiple measurements. . 29

Figure 12: Mean receptor cluster intensity is used as a measure of number of receptors trapped in cell protrusions over time due to (DPPC) immobile and (POPC) mobile ligands in bilayer. The data was fit to a numerical 2D diffusion model, in which receptors get trapped in cell protrusions. For DPPC the numerical model was fit up to 3 seconds and for POPC up to 1.5 seconds. The extracted diffusion coefficients for data presented here were 0.26 $\mu m^2 s^{-1}$ and 0.13 $\mu m^2 s^{-1}$for DPPC and POPC respectively. Right row depicts (A) analyzed cell on DPPC bilayer and evolved free receptor concentration after (B) 0.15 seconds and (C) 1 second. Color bar applies to (B) and (C). Bar = 5 μm..... 30

Figure 13: Model system to investigate FasL and IgE receptor dynamics. Palmitoyl oleoyl phosphatidyl choline (POPC) lipid bilayers are deposited via the vesicle fusion method onto a glass substrate. These bilayers also contain a pre-determined amount of dintrophenol (DNP), a model antigen. RBL mast cells were stably transfected with a FasL:GFP construct, and were also exposed to DNP-specific IgE molecules, labled with Dy520 fluorescent dye (Dyomics), before coming into contact with the bilayer. The TIRF excitation beam is directed from the bottom, through the glass substrate, producing an evanescent field at the bilayer/cell interface. 31

Figure 14: TIRF microscopy images of RBL mast cells transfected with GFP:FasL (green) and labeled with Dy-conjugated IgE molecules (red). In (A), cells were allowed to adhere to a POPC lipid bilayer containing 25 mol-% DNP antigen. In (B, left and middle), RBL cells are shown adhered to immobilized DNP-coated substrates and on untreated glass (B, right). Scale bar is *ca.* 10μm. 32

Figure 15: Single cell degranulation assay. At left, TIRF images reveal degranulation events (shown in green) in RBL cells transfected with FasL:GFP. Initial behavior is captured at > 10fps, as cells come in contact with DNP-containing POPC lipid bilayers. At right, signal intensity profiles are plotted at three individual pixel locations over time. Note the signal "bursts" as secretory lysosomes fuse with the cell membrane, releasing their contents into the cell-bilayer interface. 33

Figure 16: Quantification of FasL degranulation rate. At top, the total number of degranulation events is quantified and normalized by the total acquisition time to estimate the FasL exocytosis rate (note the colorbar below). There is a clear increase in degranulation rate with increase in the DNP antigen. At bottom, the average degranulation rate per square micron of cell membrane

rate is plotted. The large error bars indicate relative heterogeneity of FasL degranulation on a cell-to-cell basis, illustrating the stochastic nature of immune signaling. 34

Figure 17: Silver stained SDS-PAGE gel (15%T) showing purified LPS from *E. coli* and *Y. pestis* grown at 37°C. 250pmol per lane were loaded on the gel. Laddering in *E. coli* lane is indicative of typical smooth (with O-polysaccharide) LPS, while *Y. pestis* produces rough LPS. Lack of additional high or low MW bands indicates absence of protein contaminants. 36

Figure 18: Labeled LPS bound to 10μm polymyxin B-coated microspheres. 100nM Alexafluor-labeled LPS was incubated with polymyxin B-coated microspheres for 30min then microspeheres were washed and imaged to assess binding efficiency/specificity, lack of aggregation, and spectral overlap. 37

Figure 19: Dose-dependant binding of Alexa-647-labeled LPS. P388D1 murine macrophage-like cells were incubated for 15min with 100 or 500nM Alexa 647-labeled *E.coli* LPS, washed, then analyzed by flow cytometry. Note that the 100nM concentration used in subsequent TIRF imaging experiments is below saturation under these conditions..... 38

Figure 20 RAW264.7 murine macrophage-like cells were stimulated with the indicated dose and type of LPS in 96-well microtiter plates for 18hrs. Supernatants were assayed for TNFα by standard ELISA. Figure is representative of three experiments. 38

Figure 21: Dual color TIRF images of E. coli or Y. pestis LPS bound to transfected HEK-293 cells. Note aggregation of TLR4/LPS complexes in the plasma membrane. 39

Figure 22: An aggregate of helices forms (right) starting from a random configuration (left) of 40 alpha helices in a lipid bilayer (not shown). 41

Figure 23: Plot of mean squared displacement as a function of the simulation frames (10000 time steps) for 10 (black), 20(blue), 30 (red) and 40 (green)..... 42

TABLES

Table 1: Flow cytometry-based quenching assay results 23

NOMENCLATURE

BSA	Bovine Serum Albumin
DNP	Dinitrophenyl
DOE	Department of Energy
EM-CCD	Electron Multiplied Charge Coupled Device
FasL	Fas Ligand
ICS	Image Correlation Spectroscopy
IgE	Immunoglobulin E
LJ	Lennard-Jones interactions
LPS	Lipopolysaccharide
MIRR	Multi-subunit Immuno-Recognition Receptor
RBLs	Rat Basophil Leukemia Cells
SNL	Sandia National Laboratories
TEM	Transmission Electron Microscopy
TIR	Total Internal Reflection
TIRF-M	Total Internal Reflection Fluorescence Microscopy
TLR4	Toll-like Receptor 4

1. INTRODUCTION

This SAND Report presents select results from the LDRD "Resolving Dynamics of Cell Signaling via Real-Time Imaging of the Immunological Synapse" funded from FY07 through FY09. The interaction between a cell and a pathogen or stimulatory ligand begins at the "immunological synapse," the contact region of the cell and its antigen presenting surface such as and adversary or a collaborative cell. Cellular response to infectious agents is a signal transduction process that is determined not only by the presence of specific receptor proteins in the membrane, but also on the dynamics of interaction of those proteins with other key components in the signaling network. Although many proteins have been identified in the signaling machinery of various cell systems, little is known about the overall spatial organization and dynamics of protein interactions at the membrane interface during stimulation. This lack of knowledge severely limits our understanding of the critical initial phase of infectious disease processes. To address this knowledge gap we developed methods to optically detect and track in real time protein migration and clustering at membrane interfaces. Specifically, with dual color, high speed total internal reflection microscopy (TIRF-M) we can selectively excite multiple fluorophore-labeled proteins at the synaptic contact region. By coupling TIRF with advanced quantitative analysis techniques such as image correlation spectroscopy and single particle tracking we have visualized membrane reorganization upon cellular stimulation by antigen. We studied two cellular signaling networks: the IgE receptor signaling network of mast cells which is a key transduction network for allergic response and the Toll-like receptor (TLR4) response of macrophages stimulated by bacteria. Using two-color labeling schemes and our dual color TIRF-M technology we have directly monitored specific protein-protein interactions leading to cellular signaling. A modeling effort increased our ability to simulate protein behavior in a lipid environment. Overall, this project has been extremely successful in its goals to 1) provide a deeper fundamental understanding of the initial stages of cellular response to external agents in both receptor systems studied and 2) Increase SNL's core competencies in cellular signaling and visibility in the external cellular signaling community.

2. DEVELOPMENT OF IMAGING AND ANALYSIS CAPABILITIES

2.1 Total Internal Reflectance Fluorescence (TIRF) Instrumentation

We have designed and implemented a TIRF microscope that offers significant advantages over commercially available TIRF microscopes. This includes increased flexibility in both excitation and emission wavelengths, simultaneous dual color-operation, sensitivity, and acquisition speed. We have coupled this microscope with Matlab-based software to perform a variety of image preprocessing and analysis functions. These advances are detailed in the sections that follow.

2.1.1 TIRF Principles

Snell's law provides a useful framework to describe the refraction of a beam of light through two media of differing refractive indices:

$$n_1 \sin\theta_1 = n_2 \sin\theta_2 \qquad (1)$$

Where n_1 and n_2 are the refractive indices of the two media in question, with θ_1 and θ_2 describing the propagation directions of the beam in each media, with respect to the normal of the two media's interface. A peculiarity arises when the beam of light passes from a material of high refractive index (n_1) to low refractive index (n_2). In this case, as θ_1 increases, the corresponding θ_2 transitions from a real value to an imaginary one, and conventional refraction ceases. The angle at which this transition occurs is defined as the critical angle (θ_c) and can be calculated as:

$$\theta_c = \sin^{-1}\left(\frac{n_2}{n_1}\right) \qquad (2)$$

For media of sufficiently different refractive indices, this condition can happen at relatively shallow angles; for instance, for a water-glass boundary, θ_c is approximately 61 degrees. Above this angle, light is said to be under a ***total internal reflection*** condition. Although no conventional refraction through the second media occurs above this angle, continuous boundary conditions do still exist, as required by Maxwell's equations. This manifests itself as the so-called "evanescent" wave. This light wave propagates in a direction normal to the interface, and its intensity decreases exponentially with distance from its surface. The entire derivation of the evanescent wave vector is beyond the scope of this report; however, it is instructive to consider the evanescent field decay constant (d), as a function of refractive indices (n_1 and n_2), wavelength (λ), and incidence angle (θ_1):

$$d = \frac{\lambda}{4\pi\left(n_1^2 \sin^2\theta_1 - n_2^2\right)^{1/2}} \qquad (3)$$

This shows that two factors can affect the decay constant: illumination wavelength and incidence angle. As can be seen, longer illumination wavelengths and/or incidence angles near the critical angle will result in a slower decay of the evanescent field. However, under normal conditions, and for visible spectrum light (400-800nm), the decay constant is generally on the

order of 100nm, ***well below the theoretical axial resolution*** of a typical microscope. This phenomenon has spurred the development of ***total internal reflectance fluorescence (TIRF) microscopy*** as a novel method for probing interfacial phenomena. The narrow excitation field provided by the evanescent wave allows for selective excitation of chromophores very near a refractive interface. In the biological sciences, this takes particular relevance, as TIRF provides a method to image cell membrane contacts with an underlying supported substrate (such as proteins, lipids or other active molecules) (Axelrod et al., 1984). Figure 1 illustrates this concept:

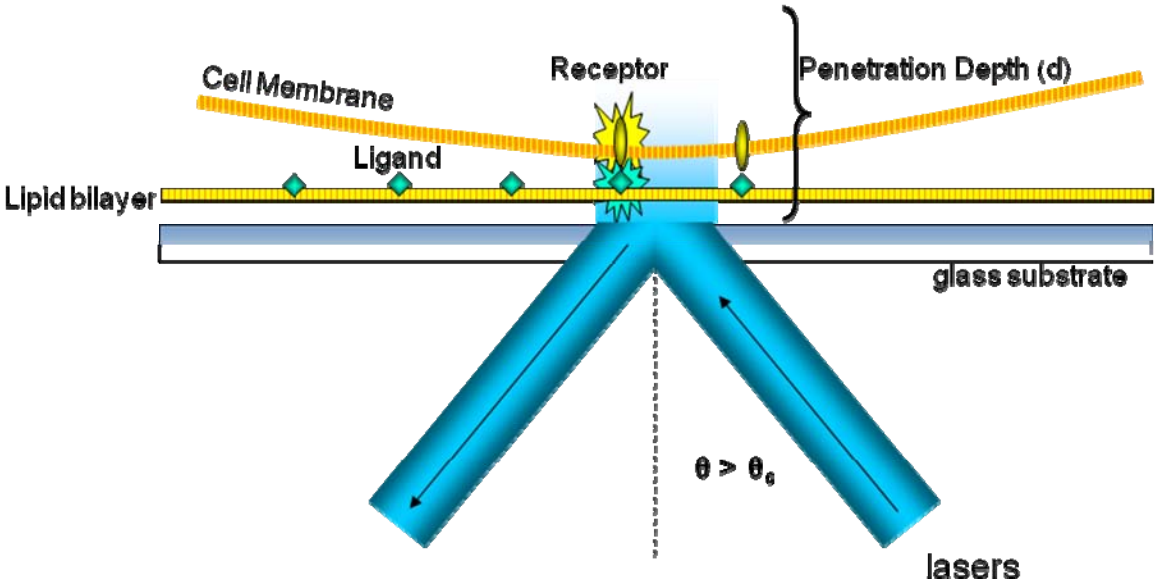

Figure 1: TIRF concept. A laser light source is directed at an oblique angle, and refracted through a glass substrate. At incident angles greater than the critical angle, light is totally internally reflected, producing a narrow evanescent field that illuminates only the first *ca.* 100nm of the sample above the glass. This geometry is ideal for investigations involving interfacial phenomena, such as ligand-membrane receptor binding in cells. The overall penetration depth of the evanescent field is a function of both the illumination wavelength and the incident angle.

2.1.2 Instrumentation

TIRF microscopy is generally accomplished through two differing approaches: (1) laser illumination is introduced onto the sample via refraction through a prism into an aqueous sample, whereby total internal reflectance (TIR) occurs at the prism-sample interface, or (2) laser illumination is focused near the periphery of the back aperture of a high NA objective, and the TIR condition occurs at a sample-coverslip interface. While the prism approach is eminently useful, the objective approach provides for certain advantages. Firstly, using an objective to direct the illumination allows for an epi-illumination geometry, thereby freeing the transmission axis for brightfield illumination and detection to compliment fluorescence images. Secondly, optical alignment is generally simpler, as the microscope objectives are generally well-aligned with the optical axis in commercial microscopes. The disadvantage of an objective-based TIRF scope, however, still remains the increased cost (Axelrod et al., 1984).

Our current setup expands upon the general TIRF microscope geometry, allowing us increased flexibility in imaging multiple species in the same field of view simultaneously. Figure 2 illustrates the optical configuration currently in use. At right, in addition to the more commonly used single-wavelength excitation, we have added a dual-wavelength illumination capability (either at 488nm and 532nm or 488nm and 633nm, respectively). This allows us two advantages that are unavailable with a single laser. First, we can excite two different fluorescent probes simultaneously. While large Stokes' shift dyes (like DY520xl commonly used in our IgE receptor experiments) can facilitate excitation and detection of two dyes using a single laser, the addition of a second wavelength dramatically increases the possible number of dyes and biomolecules compatible with our microscope. Second, as can be seen in equation (3), the penetration depth of the evanescent field is a function of wavelength. By adding a second wavelength, we are able to probe the sample at multiple depths simultaneously. The existing TIRF-M set-up can also be used in the more traditional single laser excitation configuration with any of the three excitation wavelengths.

Typically, fluorescence emission is passed through a filter to select for a wavelength region of interest and projected onto a CCD detector. In this arrangement multiple emissions are accommodated in a sequential fashion by changing the filter. Though this process can be automated, it limits the temporal resolution and is incompatible with our desire to image membrane *dynamics* in living cells. To detect multiply emitting fluorescent species simultaneously in a sample, we have also included an Optosplit image splitter (Cairn Research), as seen in Figure 2 below. This spectrally separates the fluorescence emission, and projects both images onto distinct regions of the CCD detector, thus allowing us true simultaneous dual color imaging. For instance, we can image a GFP-tagged receptor and its ligand (labeled with an organic dye such as AlexaFluor532) without switching filter sets. In addition, the Optosplit filter cube is integrated via a kinematic positioner and therefore simple to remove and replace, proviing us excellent flexibility in our emission wavelength regions. For all of our studies we employ an ultra-sensitive, 12-bit electron multiplying CCD (EMCCD, Andor), which, via an electron cascade, allows very weak signals to be amplified above the read noise of the camera, thus greatly enhancing sensitivity down to the single molecule level without significantly sacrificing speed or sensitivity (Robbins and Hadwen, 2003).

Future enhancements are currently under development for this system. As previously mentioned, the use of multiple wavelengths allows us to probe different depths within the sample. However, a more sensitive and flexible approach would be to modulate the incident angle of each laser (see equation 3). We are currently looking to utilize a set of piezo-actuated mirrors to vary the TIRF angle in a reproducible fashion, thus allowing us to extract previously unattainable information about the axial position of fluorophores at the interface.

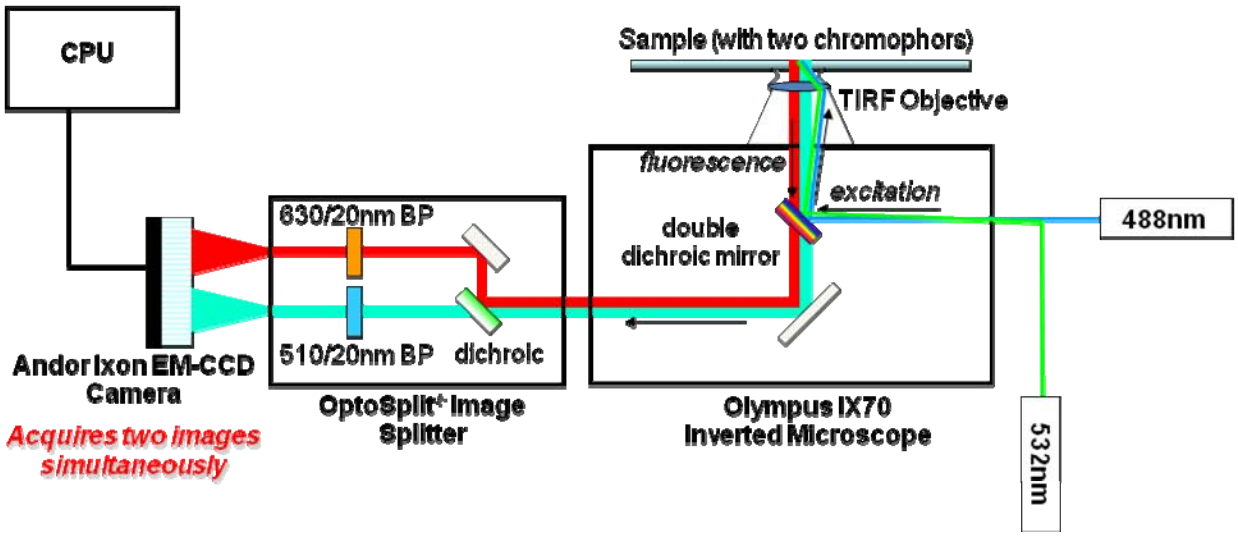

Figure 2: Optical setup of our multi-color TIRF microscope. Up to two different wavelengths can be introduced onto the sample simultaneously. The high-NA TIRF objective focuses the lasers at an oblique angle, thus producing the total internal reflectance condition. Emitted fluorescence (red and green-blue lines) can be spectrally separated using the Optosplit image splitter (Cairns Research), and projected onto spatially distinct regions of the EMCCD camera (Andor).

2.2 Image Analysis Software

We have continually developed image analysis software throughout this project to provide qualitative and quantitative information from the TIRF-M images. Primarily this software exists as standalone Matlab routines, or functions within the DIPImage toolbox for Matlab (Delft University). We have made these routines available to our collaborators throughout the project and will continue to do so. In addition to Matlab we have also utilized Image ProPlus (Media Cybernetics) and ImageJ (NIH) software packages.

2.2.1 Automated Image Alignment and Calibration

The use of the OptoSplit image splitter presents a unique challenge for image analysis. The red and green channel images appear side-by-side on the detector, however they may appear with a vertical and/or horizontal offset from each other and must be precisely realigned with respect to one another before any two-color analysis can be applied. This offset is dependant on filter alignment within the OptoSplit and therefore varies with each change in filter configuration and even slightly from day-to-day presumably due to relaxation and temperature affects. To accomplish the channel alignment we acquire an image of 0.2 µm diameter beads which are coated with a broad emission fluorophore that emits fluorescence in both of our image channels simultaneously. The resulting image is then subject to a local background subtraction to remove any local effects due to fluorescence of the mounting medium and potentially uneven illuminate. The X & Y coordinates of the beads are independently identified in each of the two image channels in the background corrected image and then a 2D transformation is calculated to adjust one channel to the coordinates of the other. This process itself has been automated and requires

no user input. Due to the excellent ability to localize points of light below the diffraction limit, the alignment of the images is accurate to within ~30 nm as determined by repeat measurements on the same calibration sample. We have developed additional Matlab functions that take this transformation and apply it to entire directories of images and/ or time-lapse sequences quickly and then outputs the resulting images and image sequences as single or color overlay *.tiff formatted files and *.avi formatted files, respectively.

2.2.2 Quantitative Image Analysis

Throughout the project we have strived to develop robust analysis tools for extracting quantitative information from our image data. We have implemented existing published algorithms as well as written new algorithms in Matlab to perform particle tracking, autocorrelation analysis, cross correlation analysis, as well as standard image processing functions such as selecting regions of interest and image statistics. Due to space limitations not all these accomplishments are detailed in this section of this report. Instead, select, relevant key developments are discussed with their applications. For additional details please see Section 3.3.2 for a discussion of improved methods for noise removal in image correlation analysis as well as Section 3.4.3 for quantification of exocytosis events.

3. IMAGING IGE IMMUNE RESPONSE IN MAST CELLS

FcεRI dynamics are well studied, yet not fully understood. Evolutionarily, immunoglobulin switching to IgE is believed to have occurred in response to parasitic helminth infections (Geha et al., 2003). However, in populations where these infections are not prevalent, IgE is implicated in allergic disease as it triggers mast cell degranulation in response to environmental and food allergens. FcεRI on the mast cell surface binds to IgE and becomes crosslinked upon binding a multivalent antigen. Crosslinking initiates a downstream signaling cascade through recruitment of the kinases Lyn and Syk which serve to propagate phosphorylation events that result in degranulation. This process is intricately woven in space and time to local membrane composition, antigen mobility, cytoskeletal restrictions, and downstream signaling proteins. We have chosen to study several of these (actin cytoskeleton dynamics, antigen mobility, and spatial-temporal receptor reorganization) as part of this project. Our major research achievements in these areas are detailed in the sections below.

3.1 The Actin Cytoskeleton and FcεRI Dynamics

The actin cytoskeleton has been implicated in restricting diffusion of plasma membrane components. RBL-2H3 mast cells transfected with GFP-actin were used to directly visualize confinement zones that restrict movement of the high affinity IgE receptor, FcεRI. Receptors were primed with quantum dots conjugated to IgE (QD-IgE), providing monovalent, non-activating probes for single particle tracking (SPT). GFP-actin and QD-IgEs were imaged simultaneously on live cells using TIRF-M. In resting cells, most IgE receptors were highly mobile over subsecond time scales within corrals of up to one square micron that were spatially defined by the actin cytoskeleton. A small fraction of receptors exhibited less mobile behavior. Dynamic reorganization of actin structures was observed over time scales of 1-10 seconds, thus making the location and dimensions of corrals time dependent. Treatment with phorbol myristate acetate (PMA) induced stress fiber formation, forming more stable corrals. An outer leaflet glycophosphatidylinositol (GPI)-anchored protein, Thy-1, was confined within subcompartments of actin-based corrals, suggesting that other membrane features may regulate diffusion within these zones.

A complete summary of the investigation of actin cytoskeleton and FcεRI dynamics has been published in a high profile journal (Andrews et al., 2008a).

3.2 The Mast Cell Synapse

The T cell receptor and B cell receptor are involved in the formation of immunological synapses with antigen presenting cells to mediate signaling and subsequent immune responses (Dustin, 2008;Ma et al., 2008;Sohn et al., 2008). The synapse itself has been well studied and consists of a centralized concentration of receptors surrounded by a peripheral ring of integrin molecules that also serve to strengthen the interaction between the two cells as well as the resulting signal (Dustin, 2008;Tolar et al., 2008). Recent findings that mast cells directly contact antigen presenting cells for signaling indicates that it is possible that mast cells also form synapses for

immune cell signaling (Perrigoue et al., 2009;Sokol et al., 2009;Yoshimoto et al., 2009). Our work has

Literature has focused on studying mast cell signaling when contacted with soluble, multivalent ligand. However, formation of a mast cell synapse would involve membrane-membrane contact mediated by IgE-ligand binding. We performed experiments to analyze FcεRI dynamics upon recognition of mobile ligand presented in a supported lipid bilayer and have shown that another member of the multi-subunit immuno-recognition receptor (MIRR) family of receptors, the high affinity IgE receptor (FcεRI), forms a synapse similar to that of the TCR and BCR upon contacting supported lipid bilayer presented ligand. Fluorescently labeled IgE was incubated with RBL-2H3 cells to allow for microscopic examination of FcεRI using TIRF-M, and Transmission Electron Microscopy (TEM) was performed to more closely examine FcεRI and other membrane components upon stimulation. We have provided the first characterization of the mast cell synapse.

3.2.1 Formation of Synaptic Regions

Rat Basophil Leukemia cells (RBL-2H3) were primed with fluorescent anti-dinitrophenyl (DNP) IgE (IgE^{DNP}) and settled onto bilayers consisting of 1-palmitoyl-2-oleoyl-*sn*-glycero-3-phosphocholine POPC and increasing mol percentages of 1,2-dipalmitoyl-*sn*-glycero-3-phosphoethanolamine-N-[6-[(2,4 dinitrophenyl)amino]hexa-noyl] (DNP-DPPE). Upon interaction between the DNP ligand within the bilayer and FcεRI-IgE^{DNP} on the cell surface, receptors were seen to coalesce into large regions in the centralized portion of the contacting cellular membrane (Figure 3). This coalescence did not occur when cells were stimulated with ligand in solution (DNP_{24}-BSA), immobilized DNP_{24}-BSA (crosslinked to the coverslip surface), or immobilized DNP-lysine (immobile monovalent ligand). In addition, if the ligand within the bilayer is presented in a manner that presents it from remaining mobile (see Section 3.3), the synaptic region also does not form. These data indicate that mobility of presented ligand is a requirement for formation of the mast cell synapse.

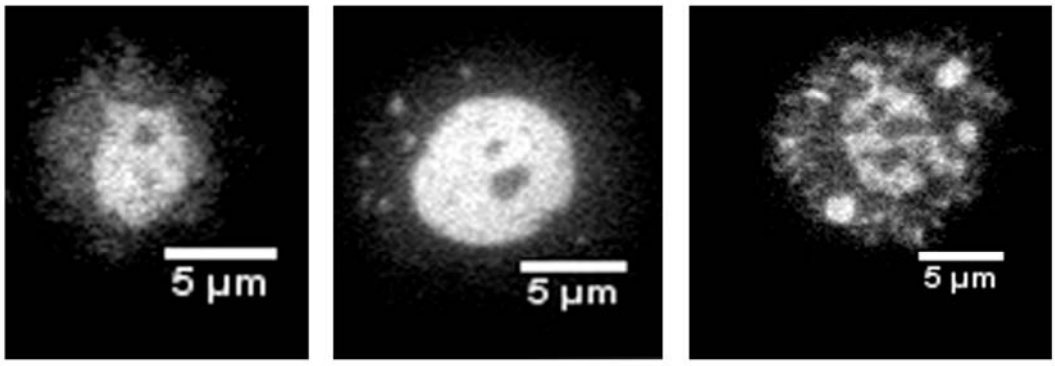

Figure 3: TIRF images of IgE^{DNP} primed cells after 12 minutes upon a 5, 10, and 25 mol% DNP-DPPE containing bilayer.

3.2.2 Mast Cell Signaling Through the Synapse

One of the hallmarks of mast cell activation through FcεRI is signaling to degranulation (Smith et al., 2003). When IgE-primed cells are stimulated with multivalent, soluble ligand that initiates receptor crosslinking (such as DNP-BSA), they secrete enzymes in a process known as degranulation. A chromagen-based assay is used to quantify the amount of enzyme that is released from mast cell granules (β-hexosaminidase) to characterize the strength of the mast cell signal in response to a given antigen. We utilized this assay to quantify the amount of β-hexosaminidase release from cells that are stimulated with supported lipid bilayer presented antigen, and compared this quantity to amounts generated by strong stimulants (DNP-BSA in solution) (Figure 4). Percent β-hexosaminidase released from cells settled onto 10 mol% and 25 mol% DNP-DPPE containing bilayers is statistically significant, but to a much lesser degree than levels occurring when cells interact with DNP-BSA in solution or immobilized to a coverslip surface. We believe that signaling within the synapse, which cannot be due to crosslinking as the ligand is monovalent, is due to mobility of the receptor within the synaptic region. As ligand bound receptors remain mobile, they can come into proximity of neighboring receptors that is sufficient to stimulate a low degree of phosphorylation eventually resulting in the decreased, yet detectable level of degranulation.

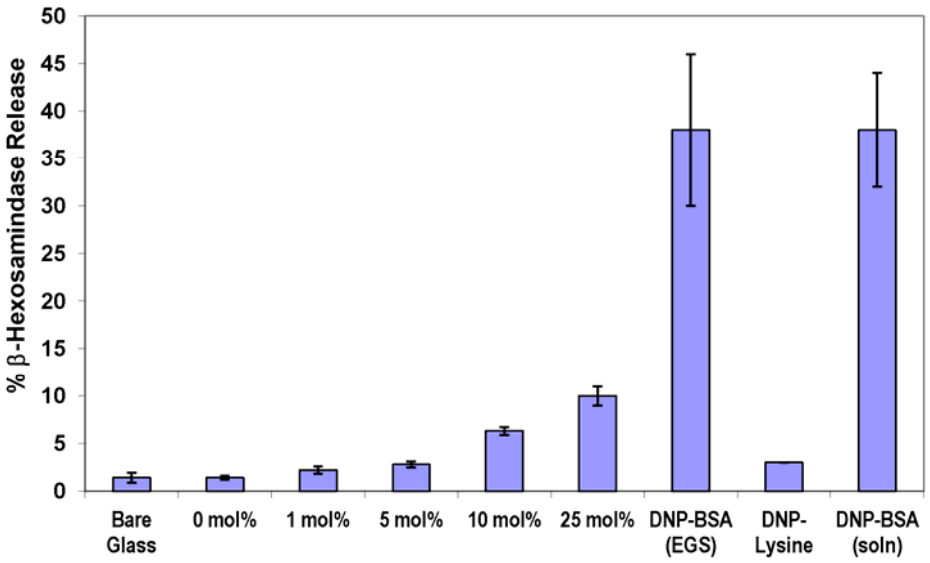

Figure 4: Degranulation assay to measure β-Hexosaminidase release from IgE^{DNP}-primed RBL-2H3 cells stimulated with mobile and immobilized ligand. Release is measured as percent total of lysate samples. Bilayers presenting 10 mol% and 25 mol% as well as soluble and immobilized DNP-BSA resulted in significant levels of degranulation above the background (spontaneous release from cells contacting glass without antigen).

To verify that the receptors remain mobile in the synapse, a region was photobleached with prolonged exposure to laser and fluorescent recovery of this region was monitored over and 8 minute period (Figure 5). Spots within the synapse recovered fluorescent signal of ~50% of original strength indicating an influx of fluorescence from the surrounding region (mobility). In

contrast, fluorescent receptor clusters formed upon contact with immobilized DNP-BSA do not recover after photobleaching.

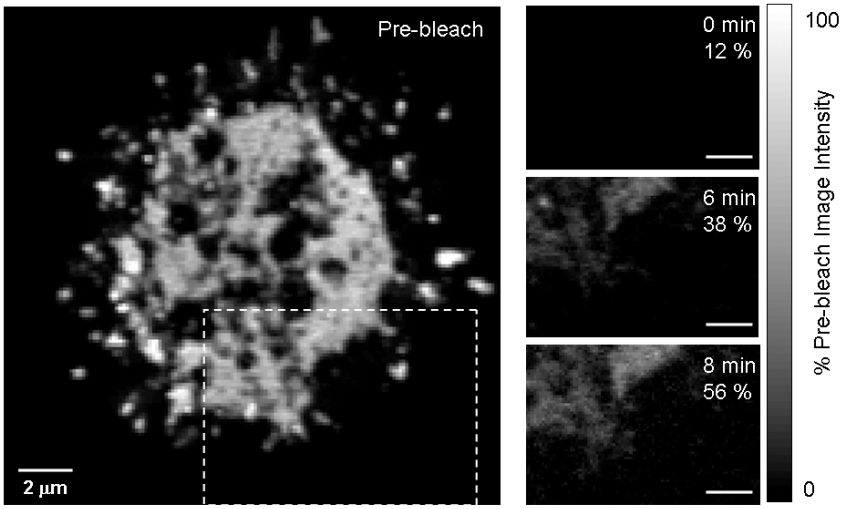

Figure 5: Fluorescent recovery within synaptic region after photobleaching. Box with dashed line represents portion of field of view photobleached. Images in the right column are the photobleached are immediate, 6 minutes, and 8 minutes post-bleach. Grayscale indicator is level of intensity within each image.

3.2.3 Cholesterol and the Mast Cell Synapse

Much experimentation has been dedicated to examining the relationship between receptors and the surrounding lipid membrane environment. Lipid rafts are believed to play a role in receptor-mediated signaling (Holowka et al., 2005;Pierce, 2002), especially in the case of FcεRI. The kinase Lyn, which phosphorylates the ITAM region of the receptor, is thought to be held in cholesterol rich domains on the cytoplasmic face of the membrane to aid in phosphorylation of the receptor upon activation (Young et al., 2003). In this manner, the lipid environment serves as a positive regulator of FcεRI signaling. In addition, activated receptor clusters and the surrounding membrane isolated from cells were found to contain high concentrations of cholesterol, commonly considered a lipid raft marker (Surviladze et al., 2007). Microscopic examination of a fluorescent lipid analog believed to colocalize with lipid rafts shows transient association with receptor clusters upon stimulation (Davey et al., 2007). Furthermore, analysis of the mast cell membrane upon receptor activation has indicated that lipid raft composition may vary between rafts by showing two raft associated proteins segregate differently within the membrane upon stimulation (Wilson et al., 2004).

All of these data indicate a potential role for lipid rafts in FcεRI signaling. One of the accepted main components of lipid rafts is cholesterol. To analyze the interaction between receptors and cholesterol within the synaptic membrane, we used a fluorescent cholesterol analog (Sato et al., 2004) to monitor localization of receptor fluorescence and cholesterol fluorescence. We first showed that the FITC-cholesterol derivative was remaining within the membrane using a flow cytometry-based quenching assay performed using a monoclonal antibody specific to the FITC

molecule (Table 1). RBL-2H3 cells either primed with FITC-IgE or replenished with FITC-cholesterol were incubated with the antibody, and then analyzed by flow cytometry. Binding of the antibody to the FITC molecule quenches fluorescence as seen in both instances with decreased counts occurring after quenching. These data indicate that the FITC-cholesterol derivative resides in the plasma membrane in an orientation where the FITC molecule remains in the extracellular space (the outer leaflet). Successful labeling of TEM membrane sheets isolating the cytoplasmic face of the membrane (the inner leaflet) with the same anti-FITC monoclonal antibody indicates that the cholesterol also flips to the inner leaflet upon repletion to become distributed through both plasma membrane leaflets. The fact that the cholesterol is located in both membrane leaflets allowed us to characterize localization in both leaflets.

Table 1: Flow cytometry-based quenching assay results

Fluorescent Label	Pre-Quench	Post-Quench
$IgE^{DNP\text{-}FITC\ (2hr\ labeling)}$	55.81	23.08
FITC-Cholesterol	72.19	27.85

TIRF and TEM allowed for microscopic examination of the localization of the cholesterol relative to FcεRI within the synaptic region (Figure 6). Two fluorescent cholesterol derivatives (FITC-cholesterol and NBD-6 cholesterol) were used to replenish cells for TIRF, but only FITC-cholesterol was used in the TEM studies (a sufficient antibody for NBD was not available). Within the synaptic region, TIRF imaging demonstrated mixing between the receptors and cholesterol on a large scale, an observation confirmed with TEM. This was different than what was seen with immobilized or soluble DNP-BSA where receptor clusters and cholesterol rarely colocalized more often remaining separated within the membrane. This separation could be due to the transient nature of a possible interaction between the two, occurring on a scale that cannot be discerned by TIRF-M or TEM (temporal or spatial).

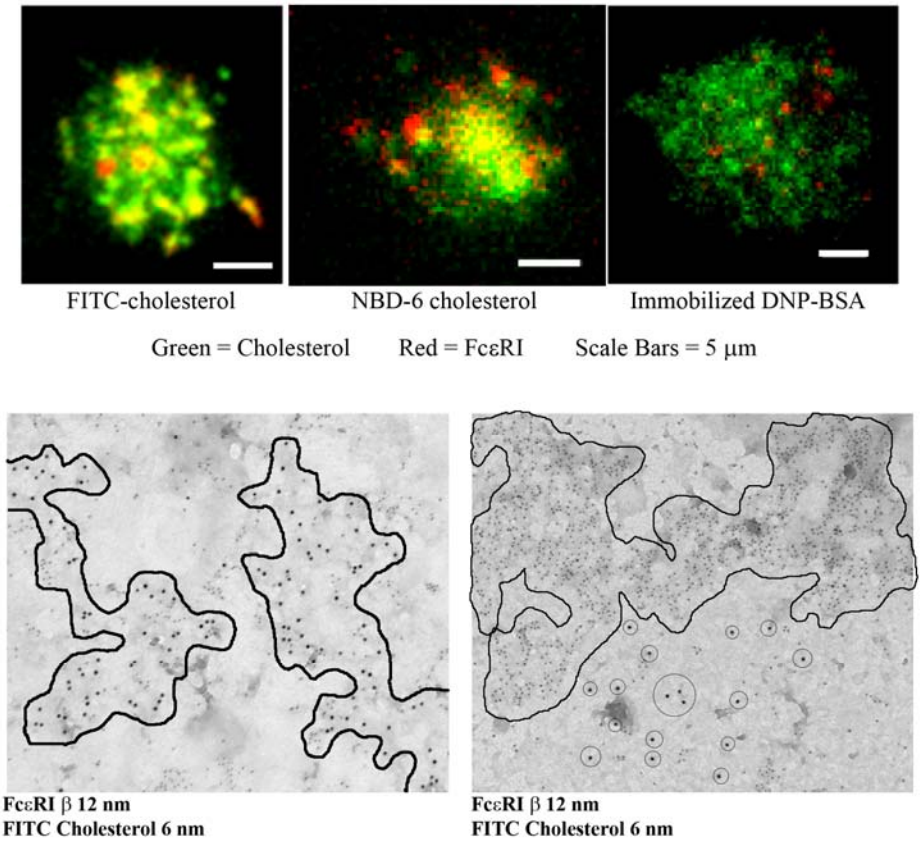

Figure 6: TIRF and TEM images of localization of cholesterol within the contacting membrane. IgE^{DNP} primed cells repleted with FITC (left image, upper row) or NBD-6 (middle image, upper row) fluorescent cholesterol and settled on 25 mol% DNP-DPPE bilayers. FITC cholesterol repleted cells primed with IgE^{DNP} were also settled onto immobilized DNP-BSA (right image, upper row). Membrane sheets from FITC-cholesterol repleted, IgE^{DNP} primed cells on either 25 mol% DNP-DPPE bilayers (left image, lower row) or immobilized DNP-BSA stained for FcεRI (12 nm) and FITC (6 nm). On sheets from mobile ligand substrate, regions containing both receptor and cholesterol are outlined. On sheets from immobilized DNP-BSA surfaces, cholesterol label is highlighted with receptor label circled in the surrounding membrane region.

Another membrane bound protein that plays a role in propagation of the FcεRI signal is Linker of Activated T cell or LAT. LAT is believed to reside in lipid rafts due to the dual palmitoylated portion of the protein. We employed TEM to characterize the localization of LAT relative to receptors in the synapse (Figure 7). Membrane sheets labeled for FcεRI β and LAT showed that large LAT domains formed within the membrane upon stimulation with bilayer presented ligand (similar to previous results with soluble ligand; (Wilson et al., 2001), but that these domains mostly remained in portions of the membrane peripheral to coalesced receptors. This is of particular interest as one would expect LAT and cholesterol to localize together as they both are lipid raft components. It is possible these results are another indication that lipid rafts actually vary within the same cellular membrane.

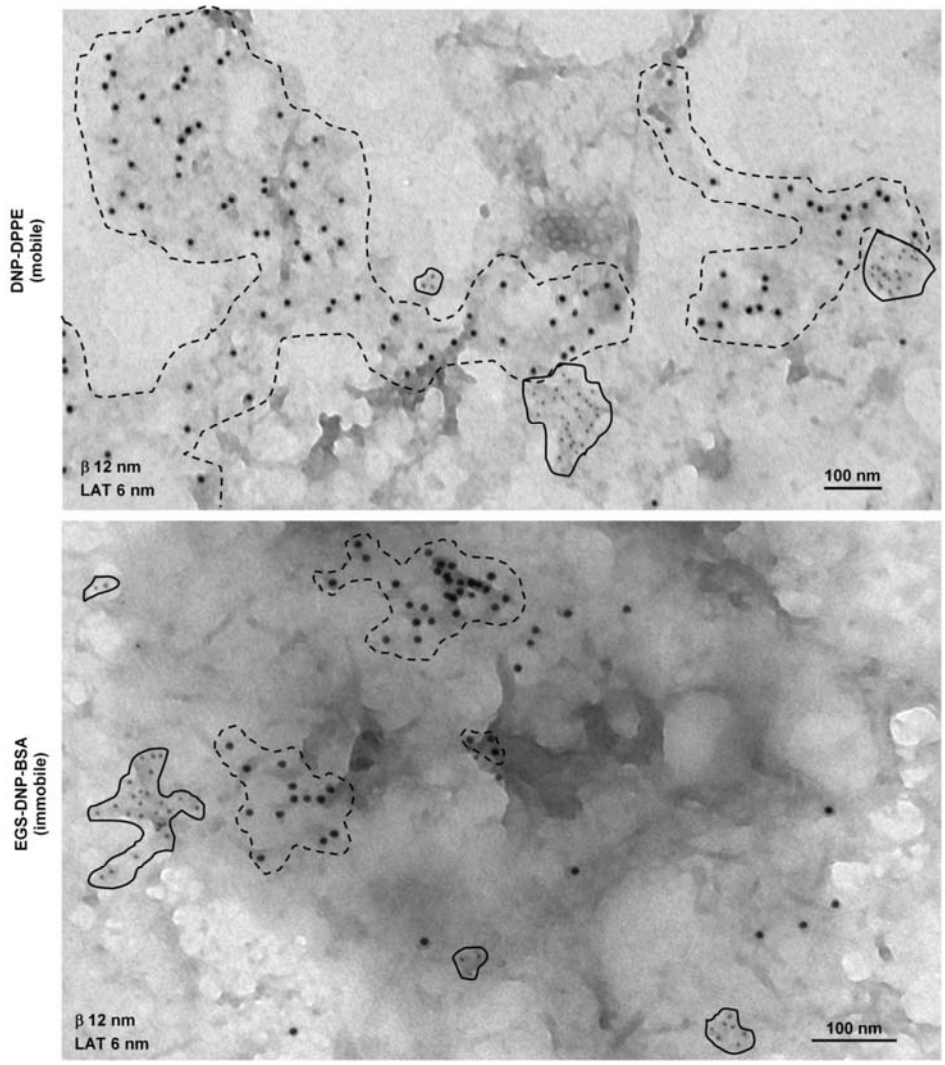

Figure 7: Localization of LAT relative to receptor in membrane sheets isolated from 25 mol% DNP-DPPE bilayers (upper image) or immobilized DNP-BSA (bottom image) surfaces. Receptors (12 nm gold) are circled with dashed lines while LAT (6 nm gold) clusters are circled with solid lines.

3.2.4 Synapse Formation Delineation by the Actin Cytoskeleton

Cytoskeletal elements have been shown to play a role in receptor mediated signaling. Current data indicates that mobility of receptor clusters formed upon stimulation of mast cells with soluble ligand is partially regulated by the underlying actin cytoskeletal structure (Andrews et al., 2008b). Namely, actin works to corral receptor clusters within certain regions of the membrane, and the dynamic nature of actin structure allows for movement of receptor clusters between domains. The actin cytoskeleton also plays a role in several other cellular processes including cell spreading, cell motility, and cell division.

To characterize the role of the actin cytoskeleton in formation of the mast cell synapse, we performed TIRF microscopy on Ige^{DNP} primed RBL-2H3 GFP-actin cells settling onto ligand

presenting bilayers (Figure 8). Over time, the actin cytoskeleton becomes localized to the periphery of the cell forming a ring around the edge. We hypothesize the structure of the actin cytoskeleton plays a variety of roles in the mast cell synapse including helping to stabilize the contact region between membranes and to maintain mobile receptors in a centralized region.

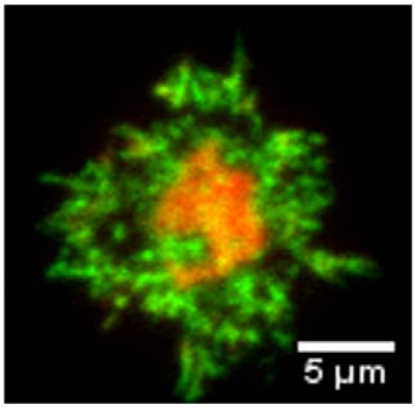

Figure 8: TIRF image of actin-GFP IgE^{DNP} primed RBL-2H3 cell settling onto a 25 mol% DNP-DPPE bilayer. Actin is green and receptors are red.

3.2.5 Synopsis

The mast cell synapse is potentially a necessary part of mast cell signaling upon engagement with antigen presenting cells. Our studies indicate that it forms when IgE-FcεRI complexes become engaged with a two-dimensionally mobile ligand. Furthermore, maintained receptor mobility is necessary for the formation of the synaptic region. Remarkably, signaling to degranulation does occur through the synapse presumably through a density associated phenomenon where receptors are simply capable of finding multiple receptor partners to complete transphosphorylation interactions. However, it remains possible that conformational changes upon ligand binding might also serve to mediate signaling through the synapse as seen with the T cell and B cell receptors. We have also characterized the roles of cholesterol and actin in formation of the mast cell synapse encouraging the further analysis of lipid raft involvement in FcεRI signaling. The mast cell synapse findings have been submitted for publication to Journal of Immunology and are currently pending review (Carroll-Portillo et al., 2009).

3.3 Mechanism of FcεRI Receptor Cluster Formation

The phenomenon of receptor cluster formation is well known and has been demonstrated experimentally in our work and that of others, however the underlying mechanism by which these aggregates form in the very early stages of their growth has not been demonstrated experimentally. We used a combination of pipette manipulation and image correlation analysis to capture the earliest events in cell membrane contact. Our results show that the receptors redistribute on the cell membrane by diffusion-mediated trapping at cell protrusions.

3.3.1 Pipette Manipulation of Cells

As is shown in Section 3.1 of this report, when RBL cells loaded with fluorescent IgE were allowed to settle onto surfaces a heterogeneous fluorescence distribution was always observed. Since cells settled under gravity, the contact area between the cell and the membrane is gradually increasing (as the cell spreads out), while simultaneously receptors are redistributing into clusters (Figure 9A, B). This makes a dynamic analysis of the clustering behavior exceedingly complex, as both new membrane area and new receptors are continually being added to the interface. To achieve a stable contact area and to precisely fix the time of first contact with the surface, a micromanipulation technique was implemented (Chesla et al., 1998). Using pipette manipulation to precisely fix the time of first contact with the surface (Figure 9C, D), the early time evolution of the fluorescence heterogeneities can be observed. TIRF-M was used to image the cells and the characteristic cluster sizes were analyzed using image correlation spectroscopy (Petersen et al., 1993).

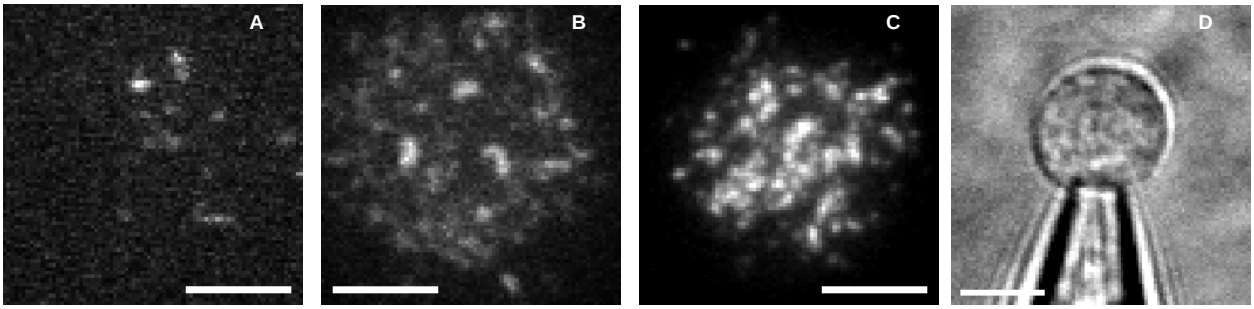

Figure 9: Top Row. TIRF images of DY520-XL-labeled IgE in receptor clusters, on a RBL-2H3 cell in contact after approximately (A) 45 seconds and (B) 5 minutes with a POPC bilayer with 10 mol% ligand lipids. Cell settled due to gravity. Bottom Row. (C) TIRF image of Alexa488-labeled IgE on a RBL-2H3 cell at initial contact with a POPC bilayer with 25 mol% ligand lipids. This cell was pushed down with a micropipette. (D) a micrograph showing a RBL-2H3 cell held approximately 1 μm above the surface with a micropipette. Bar = 5 μm

3.3.2 Image Correlation Spectroscopy with Explicit Noise Removal

Image correlation spectroscopy (ICS) was used to quantitatively measure receptor distributions on cell surfaces (Petersen et al., 1993;Wiseman and Petersen, 1999). ICS involves computing the two dimensional spatial autocorrelation function, $g(\varepsilon,\eta)$ of an image $i(x,y)$:

$$g(\varepsilon,\eta) = \frac{\langle i(x,y)i(x+\varepsilon,y+\eta)\rangle}{\langle i\rangle^2} - 1 \qquad (1)$$

In systems without orientational order, all the information in the correlation function is contained in its rotational average, $g(r)$ and the width of this distribution is a measure of the spatial scale of heterogeneities (convolved with the point spread function of the optical system.) The intensity variance includes a significant contribution from spatially uncorrelated camera read noise and shot noise. The standard procedure (Petersen et al., 1993;Wiseman and Petersen, 1999) to obtain

the noise-corrected variance is to fit data near the origin to the autocorrelation of the point spread function (PSF) itself if the PSF is larger than one pixel. In our case, a large field of view prevents oversampling and the noise corrected autocorrelation $g_s(0)$ is obtained by direct removal of camera read noise σ_r, and shot noise σ_p:

$$g_s(0) = g(0) - \frac{\left\langle s_r^2 + s_p^2 \right\rangle}{\left\langle i \right\rangle^2} \quad (2)$$

This approach has previously been applied to the "number and brightness" (N&B) analysis (Digman et al., 2008;Unruh and Gratton, 2008) but not to ICS.

3.3.3 Initial Receptor Clusters Form at Cell Protrusions by Diffusion-Mediated Trapping

To characterize the heterogeneous distribution of fluorescent IgE receptors, the rotationally averaged image correlation function was computed. To eliminate artifacts from the finite cell size, each image was padded outside the cell with the cell mean intensity. Figure 10 shows a typical image and correlation function.

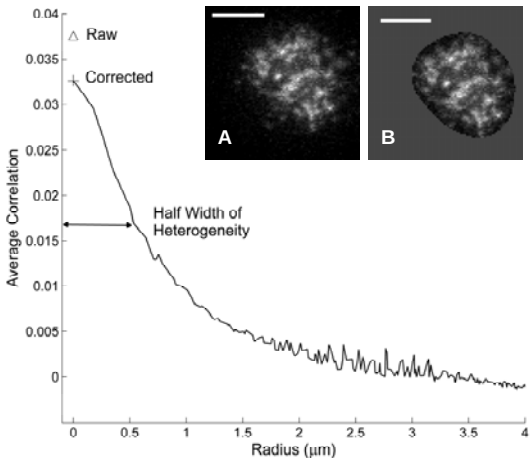

Figure 10: Image correlation was performed to determine the size of heterogeneity and g(0) of single cells pipette-pressed against a stimulating surface. Rotationally averaged correlation showing explicit noise removal and half width of receptor clusters. Inset (A) is TIRF image of RBL cell and (B) is same image masked with mean of cell interior analyzed here. Bar = 5 µm.

The exponential decay of the evanescent field can result in heterogeneous fluorescence intensity even on membranes with uniform receptor distributions, if the membrane itself has regions that are much more closely apposed to the substrate. Hence, we interpret the heterogeneities on surfaces as points of close contact between the cell and the surface. This interpretation is supported by previously published studies using scanning electron microscopy (Hamawy et al., 1992). Quantitatively, the spatial scale of the heterogeneities, as assessed by the width of the

correlation function at half maximum, showed no statistically significant differences on different surfaces, as shown in Figure 11.

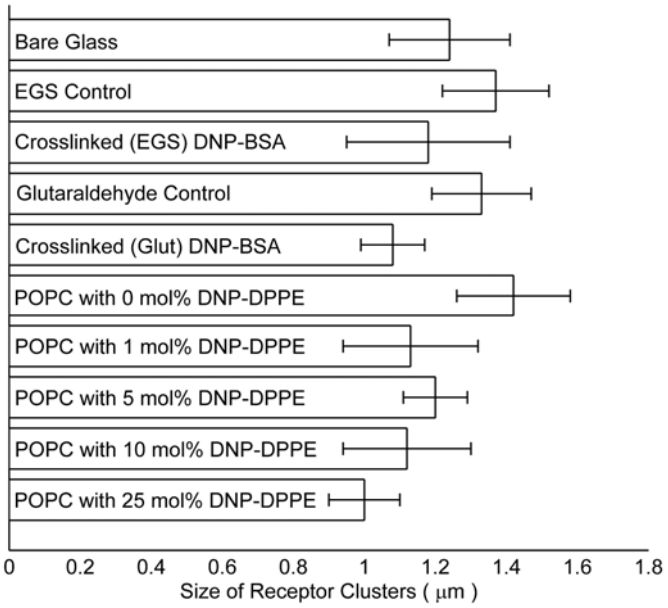

Figure 11: Size of IgE receptor heterogeneities on different surfaces within five seconds of contact. The spatial scale of heterogeneities is the same for crosslinked DNP-BSA and their control surfaces which suggests that the mechanism of IgE receptor aggregation is trapping at cell protrusions. The error bars represent the standard deviation from multiple measurements.

The similarities between heterogeneities observed on different surfaces, including surfaces that display no ligands for IgE, strongly support the contention that clusters of IgE receptors observed on contacting ligand-presenting surfaces are formed by diffusion-mediated trapping at points of close contact between the cell and the surface. To further test this hypothesis, we fit the rapidly increasing fluorescence in clusters to a simple finite-element diffusion model in MATLAB. Very good fits were found for immobile ligands represented in Figure 12. On mobile surfaces, fits were found to deviate slightly after several seconds; this downward deviation in the data was apparently caused by the cluster mobility. The obtained mean diffusion coefficients were $0.48 \pm 0.14\ \mu m^2 s^{-1}$ and $0.31 \pm 0.20\ \mu m^2 s^{-1}$ for immobile and mobile ligands respectively, which gave diffusion coefficients that were consistent with literature (Larson et al., 2005). The errors represent the standard error of the mean of at least three measurements.

This work is being prepared for publication in Biophysical Journal.

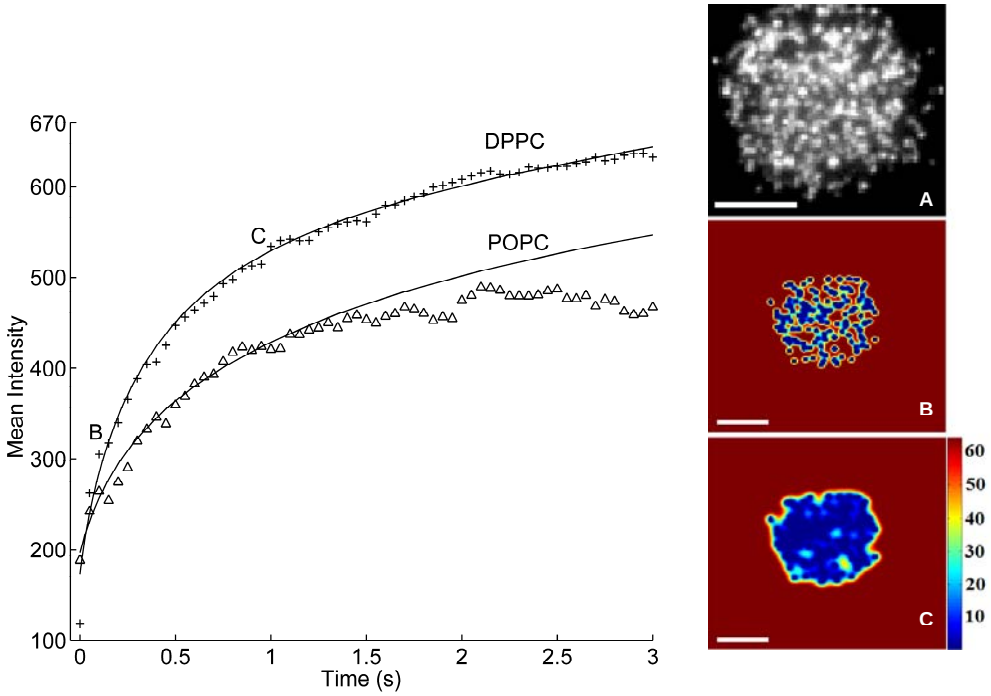

Figure 12: Mean receptor cluster intensity is used as a measure of number of receptors trapped in cell protrusions over time due to (DPPC) immobile and (POPC) mobile ligands in bilayer. The data was fit to a numerical 2D diffusion model, in which receptors get trapped in cell protrusions. For DPPC the numerical model was fit up to 3 seconds and for POPC up to 1.5 seconds. The extracted diffusion coefficients for data presented here were 0.26 $\mu m^2 s^{-1}$ and 0.13 $\mu m^2 s^{-1}$for DPPC and POPC respectively. Right row depicts (A) analyzed cell on DPPC bilayer and evolved free receptor concentration after (B) 0.15 seconds and (C) 1 second. Color bar applies to (B) and (C). Bar = 5 μm.

3.4 Development of a Single-Cell Degranulation Assay

We chose to study the dynamics of the high-affinity IgE receptor (FcεRI) and the Fas ligand in mast cells (Kinet, 1999;Smith et al., 2003) following exposure to the antigen dinitrophenol (DNP). This system represents a well-studied, yet not fully understood molecular mediator of acquired immune system stimulation. Receptor dynamics and secretory vesicle trafficking were followed simultaneously in living cells with TIRF-M.

3.4.1 Model system for Visualization of Degranulation

The apoptosis-causing Fas ligand (FasL) provides a convenient tool to study degranulation dynamics, as it has been shown to be targeted to secretory lysosomes within mast cells. Following antigen stimulation and receptor crosslinking the intracellular signaling cascade is initiated. This cascade results in secretory vesicles fuse to the cell membrane and release their contents into the extracellular space (Smith et al., 2003). While the identity of these and other molecular players are known, as well as their relative roles in immune response signaling cascades, relatively little work has been done in studying immune response in the stochastic

regime. Optical microscopy provides an opportunity to evaluate single cell behavior, thus providing a more complete, nuanced view of this system. TIRF-M, in particular, lends itself well to such studies of membrane-associated proteins, as it confines the excitation to the cell-antigen interface (Axelrod, 2001). Figure 13 illustrates the model system used in these studies.

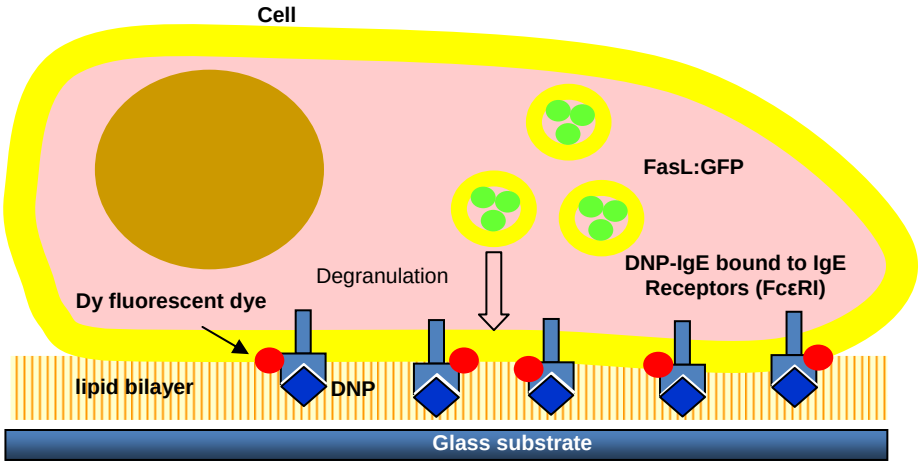

Figure 13: Model system to investigate FasL and IgE receptor dynamics. Palmitoyl oleoyl phosphatidyl choline (POPC) lipid bilayers are deposited via the vesicle fusion method onto a glass substrate. These bilayers also contain a pre-determined amount of dintrophenol (DNP), a model antigen. RBL mast cells were stably transfected with a FasL:GFP construct, and were also exposed to DNP-specific IgE molecules, labled with Dy520 fluorescent dye (Dyomics), before coming into contact with the bilayer. The TIRF excitation beam is directed from the bottom, through the glass substrate, producing an evanescent field at the bilayer/cell interface.

3.4.2 FasL:GFP Dynamics During Cell Stimulation

We synthesized supported Palmitoyl oleoyl phosphatidyl choline (POPC) lipid bilayers containing up to 25% (mol/mol) dinitrophenol (DNP). RBL mast cells previously transfected with FasL:GFP fusion protein, and incubated with Dy-IgE fluorescent conjugates, were deposited on the DNP-lipid bilayers. Due to the large Stokes' shift of the Dy dye, both fluorophors can be excited by a single 488nm laser and monitored simultaneously on a single CCD detector via an Optosplit image splitter (Cairns Research). Note the TIRF excitation is brought through the glass substrate, producing an evanescent field at the bilayer-cell boundary as described in Section 2.

Figure 14A contains TIRF-M images of IgE receptor clusters (shown in red) and FasL expression within the secretory vesicles (green). A large-scale reorganization of receptors towards the central portion of the interface is observed within 5-10 minutes of cell contact with the stimulatory substrate. This is made possible by the 2D fluidity of the DNP-containing lipid bilayer as presented in Section 3.2. Similar large-scale IgE reorganization is not observed when antigen mobility is restricted via glutaraldehyde tethering of DNP to a glass surface (B, left and middle), or if stimulated cells are in contact with an untreated glass surface (B, right).

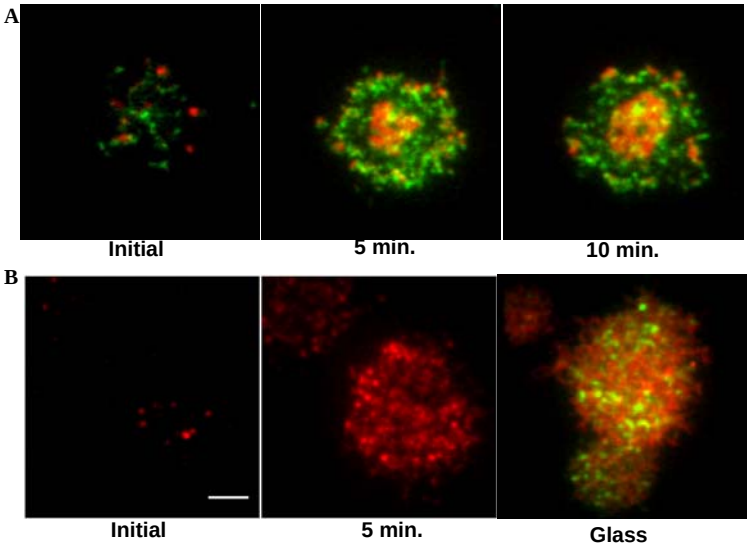

Figure 14: TIRF microscopy images of RBL mast cells transfected with GFP:FasL (green) and labeled with Dy-conjugated IgE molecules (red). In (A), cells were allowed to adhere to a POPC lipid bilayer containing 25 mol-% DNP antigen. In (B, left and middle), RBL cells are shown adhered to immobilized DNP-coated substrates and on untreated glass (B, right). Scale bar is *ca.* 10μm.

3.4.3 Quantifying Degranulation at the Single Cell Level

Figure 15, left iilustrates DNP-mediated FasL degranulation (shown in green) in RBL cells at early time-points upon contact with the DNP-lipid bilayer. Images were acquired at 10fps. Upon fusing with the cell membrane, FasL-containing secretory vesicles become apparent as "bursts" in the signal intensity over time, as shown in Figure 15, right.

Using this high resolution spatio-temporal data, we analyzed the signal time course of each pixel in the image in an attempt to quantify the FasL degranulation rate in single cells. A FasL degranulation event was detected by the following algorithm: Each pixel's value over time was normalized by its time-averaged value (typically taken over 40-50 seconds). If a pixel's value at a given time point increased from its mean value by greater than 20% of the mean, and then returned below this threshold, it was deemed to be indicative of a FasL degranulation. This threshold was chosen via visual inspection of the data. As a comparison, background pixels showed an average deviation from a mean value by no more than 3-4%.

The total number of these events was summed at each pixel, and then divided by the total acquisition time to estimate the FasL degranulation rate at each pixel in the image. This result is shown in Figure 16, top, using a grey scale colorbar. Data from cells exposed to bilayers containing 5%, 10%, and 25% DNP were analyzed, and compared to cells that were not exposed to a bilayer. The images show a clear qualitative relationship between DNP concentration and FasL degranulation rate. Figure 16, bottom shows average values, normalized by the number of pixels, for each DNP concentration.

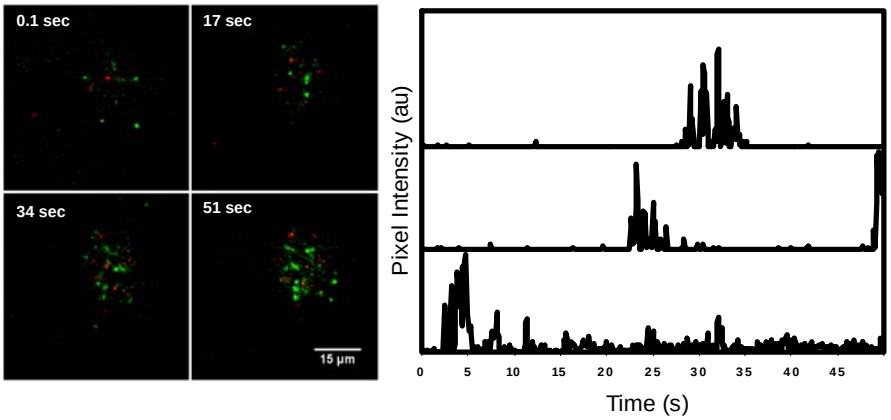

Figure 15: Single cell degranulation assay. At left, TIRF images reveal degranulation events (shown in green) in RBL cells transfected with FasL:GFP. Initial behavior is captured at > 10fps, as cells come in contact with DNP-containing POPC lipid bilayers. At right, signal intensity profiles are plotted at three individual pixel locations over time. Note the signal "bursts" as secretory lysosomes fuse with the cell membrane, releasing their contents into the cell-bilayer interface.

Interestingly, roughly a quarter of the cells studied showed little degranulation, despite the fact that FasL expression was detected. This is reflected in the relatively large error bars in the graph. This apparent heterogeneity illustrates the utility of developing imaging-based single cell approaches over bulk degranulation assays which do not reveal the stochastic nature of immune signaling.

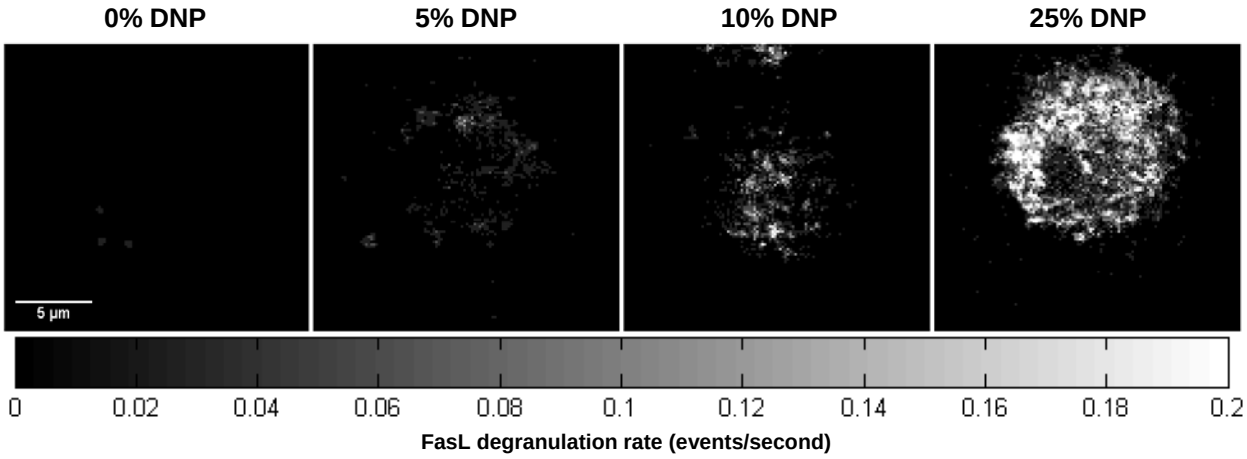

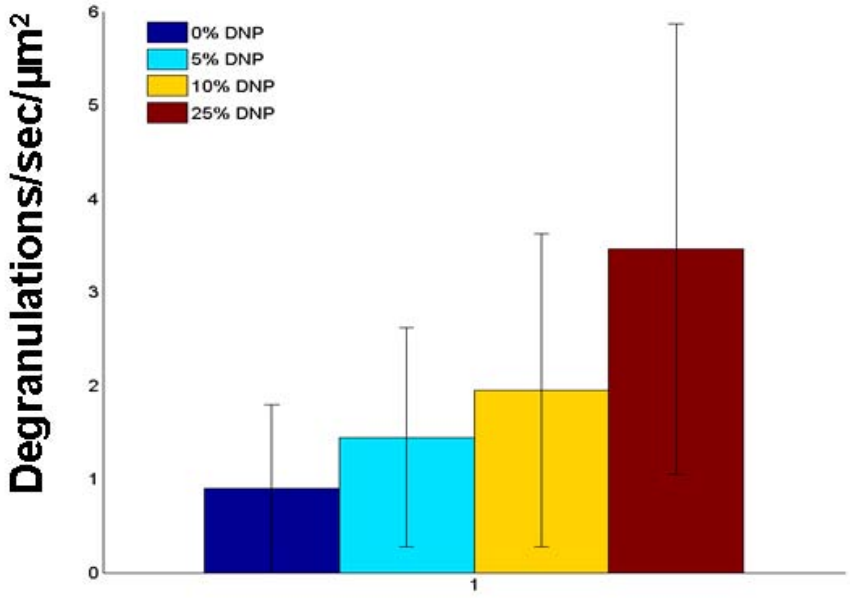

Figure 16: Quantification of FasL degranulation rate. At top, the total number of degranulation events is quantified and normalized by the total acquisition time to estimate the FasL exocytosis rate (note the colorbar below). There is a clear increase in degranulation rate with increase in the DNP antigen. At bottom, the average degranulation rate per square micron of cell membrane rate is plotted. The large error bars indicate relative heterogeneity of FasL degranulation on a cell-to-cell basis, illustrating the stochastic nature of immune signaling.

4. IMAGING OF TLR-4 RECEPTOR RESPONSE TO BACTERIAL ANTIGENS

4.1. The Role of TLR4 in Innate Immunity

The innate immune response is critical to survival of infection. Its primary functions are pathogen detection, containment, and clearance, which serve both to eliminate the invading organisms as well as to slow their proliferation long enough for the adaptive immune response to develop lasting sterilizing immunity. Clearly, early and efficient pathogen detection is key to the success of this mechanism. Among the host cell receptors responsible for sensing infection is Toll-like receptor 4, which is activated by the gram-negative bacterial outer membrane component lipopolysaccharide (LPS). LPS is an approximately 10-100 kDa macromolecule consisting of three domains: O-polysaccharide, core polysaccharide, and lipid A. It serves to strengthen the bacterial outer membrane against both environmental stresses and immune attack by antibodies and complement (Miller et al., 2005). Upon entering a mammalian host, some LPS is liberated as bacteria divide and as some are damaged by the innate immune system. This free LPS is quickly bound by LPS-binding protein which then transfers it to the TLR4 receptor complex (TLR4, CD14, and MD2) on cells such as macrophages and dendritic cells. CD14 catalyzes loading of LPS onto a hydrophobic domain of MD2 which then facilitates dimerization or multimerization of TLR4 and subsequent initiation of a signaling cascade (reviewed recently in (Carpenter and O'Neill, 2009)).

The TLR4 signaling cascade propagates through two basic branches defined by their most receptor-proximal adaptor proteins MyD88 and TRIF (reviewed recently in (Carpenter and O'Neill, 2009). Through a series of primarily phosphorylation and ubiqutination events, NF-kB and other transcription factors are activated to enter the cell nucleus. This results in rapid induction of the cellular innate immune response in which a variety of inflammatory cytokines such as TNFα and chemokines such as IL-8 are produced. These secreted factors then signal the presence of infection to nearby and distant cells of the innate and adaptive immune systems, recruiting and coordinating their activities to clear the infection.

4.2 LPS Can Be Modified to Subvert Detection

Most gram negative bacteria such as *Escherichia coli* produce LPS bearing a lipid A domain with six acyl chains. These hexaacylated LPS forms are highly potent stimulators of the TLR4 pathway. However, some pathogenic bacteria such as *Yersinia pestis* (plague) have evolved to produce a modified LPS containing tetraacyl lipid A. In the case of Y. pestis, this occurs in response to the temperature shift commensurate with transfer from the flea vector to the mammalian host (Rebeil et al., 2004). This shift in lipid A structure dramatically reduces the TLR4 stimulatory properties of LPS, rendering it less “visible” to the innate immune system. Indeed, the ability to shift from hexaacylated to tetraacylated lipid A is absolutely required for virulence (Montminy et al., 2006). However, tetraacyl LPS can still bind and stimulate TLR4 at high concentrations as well as antagonize signaling by hexaacylated LPS forms at lower doses (Flad et al., 1993). The mechanism by which these dual properties are possible is not known. We chose to investigate how each form of LPS affects localization and multimerization of TLR4

Figure 17: Silver stained SDS-PAGE gel (15%T) showing purified LPS from *E. coli* and *Y. pestis* grown at 37°C. 250pmol per lane were loaded on the gel. Laddering in *E. coli* lane is indicative of typical smooth (with O-polysaccharide) LPS, while *Y. pestis* produces rough LPS. Lack of additional high or low MW bands indicates absence of protein contaminants.

receptor complexes in order to determine whether binding and early signaling events are intact or altered in the response to *Yersinia pestis* LPS.

4.3 Purification, Testing, and Labeling of LPS

LPS from wild-type *E. coli* was purchased from Sigma. LPS from *Y. pestis* strain KIM6+ was prepared by the method of Darveau and Hancock (Darveau and Hancock, 1983). Briefly, bacteria were grown to early stationary phase at eith 21 or 37°C, lysed in a French press, and treated with RNAse and DNAse. LPS was precipitated using Mg++ and ethanol, treated with protease E, then purified by chloroform/methanol then phenol/chloroform extractions. LPS was resuspended in endotoxin-free water with 0.1% triethylamine to facilitate dispersion then quantified by the thiobarbituric acid method (Karkhanis et al., 1978) which is an assay for the kdo sugars of the core polysaccharide. Purity and quality of each preparation was assessed by SDS-PAGE and silver stain (Fomsgaard et al., 1990). Figure 17 shows a representative gel.

LPS was labeled with Alexa Fluor® 488, 555, or 647 hydrazide (Molecular Probes) as described previously (Triantafilou et al., 2000). Briefly, purified LPS was incubated with the hydrazide dye in the presence of galactose oxidase and neuraminidase to facilitate dye reaction with core polysaccharide aldehydes then quenched with sodium borohydride. To verify that labeling did not abolish specific binding, labeled LPS was incubated with microspheres coated with polymyxin B then imaged (Figure 18). Microspheres were prepared by coupling polymyxin B (Sigma) to COOH-modified 10μm polystyrene microspheres (Bangs Laboratories) using the Polylink protein coupling kit (Bang's Laboratories) per manufacturer's protocol. LPS was also

tested for binding to a macrophage cell line (P388D1) by flow cytometry under the same conditions used subsequently for TIRF imaging (Figure 19).

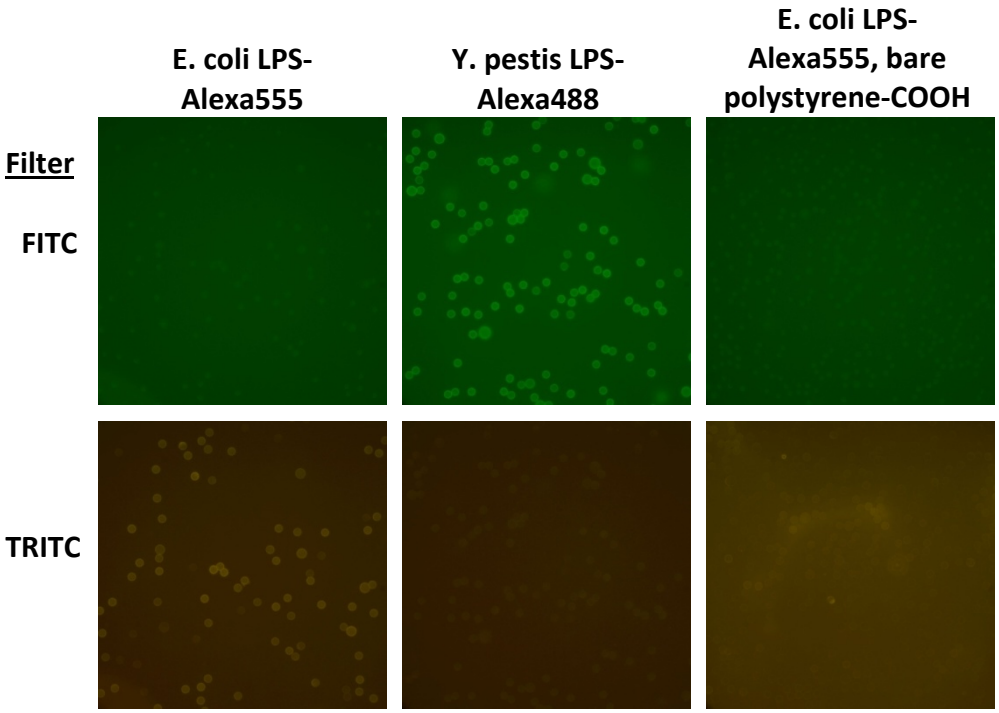

Figure 18: Labeled LPS bound to 10μm polymyxin B-coated microspheres. 100nM Alexafluor-labeled LPS was incubated with polymyxin B-coated microspheres for 30min then microspeheres were washed and imaged to assess binding efficiency/specificity, lack of aggregation, and spectral overlap.

To assess the stimulatory capacity of each LPS type, $2x10^4$ RAW264.7 macrophage-like cells per well were seeded in 96-well microtiter dishes. LPS was added at the indicated concentrations and cells were incubated for 18hrs. TNFα production was measured by ELISA (eBioscience) as shown in figure 4D. Note the approximately 100-fold difference in dose responsiveness to LPS from *E. coli* or *Y. pestis* grown at 21°C (hexaacylated) versus that from Y. pestis grown at 37°C (tetraacylated).

4.4 Simultaneous TIRF Imaging of LPS and TLR4 in Live Cells

As Figure 20 indicates, LPS responsiveness is not entirely abolished by the shift to the tetraacyl form of lipid A. In addition, other assays (NF-κB activation dynamics) suggest that even at relatively low concentrations (1nM) macrophages do respond to Y. pestis 37°C LPS, albeit with marked differences (our unpublished observations). Together, these observations suggest that tetraacylated LPS does bind efficiently to TLR4/MD2 but that there is a qualitative difference in how it interacts with the complex. One possibility is that tetraacylated LPS binds but fails to induce higher order receptor complex aggregates or membrane dynamics that may be required for efficient signaling.

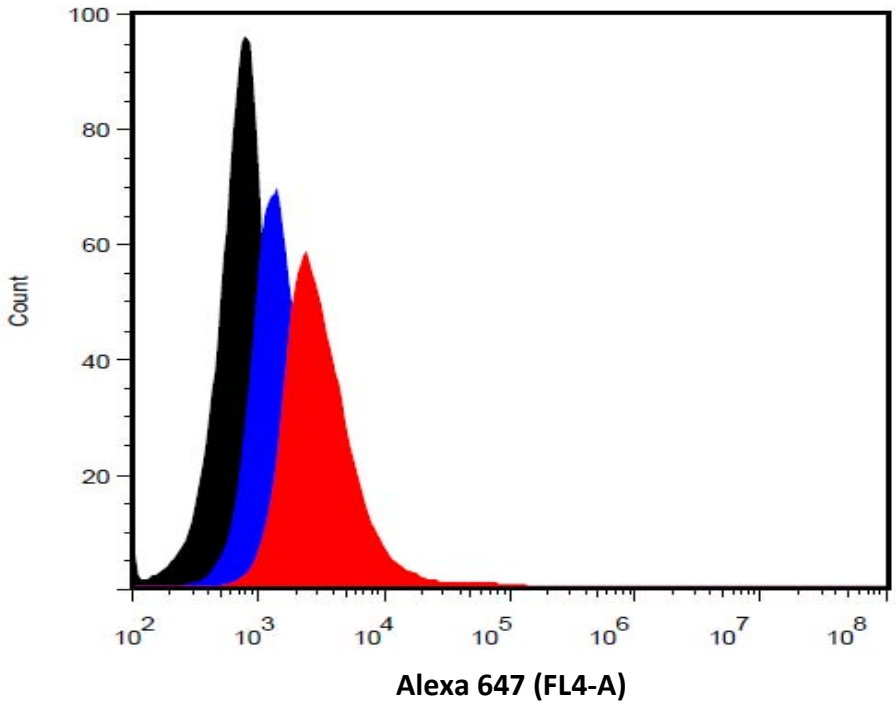

Figure 19: Dose-dependant binding of Alexa-647-labeled LPS. P388D1 murine macrophage-like cells were incubated for 15min with 100 or 500nM Alexa 647-labeled *E.coli* LPS, washed, then analyzed by flow cytometry. Note that the 100nM concentration used in subsequent TIRF imaging experiments is below saturation under these conditions.

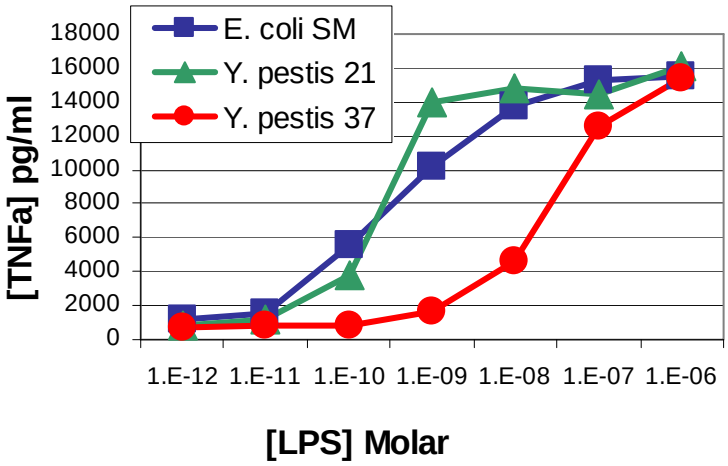

Figure 20 RAW264.7 murine macrophage-like cells were stimulated with the indicated dose and type of LPS in 96-well microtiter plates for 18hrs. Supernatants were assayed for TNFα by standard ELISA. Figure is representative of three experiments.

To test this possibility, we used simultaneous two color TIRF microscopy to assess colocalization (binding) and TLR4 aggregation and movement in the cell membrane. To visualize TLR4 without the interference of bound antibodies, we generated a cell line expressing YFP:TLR4 with YFP at the cytoplasmic amino terminus of the protein. The plasmid containing YFP:TLR4 (a kind gift of David Segal (Visintin et al., 2001)) was linearized using ApaLI. HEK-293 cells stably expressing human MD2 and CD-14 (Invivogen) were grown in DMEM/10% FBS and transfected with the linearized plasmid using the Amaxa Nucleofector® and Kit V reagents. Cells were selected for integration and expression by culturing for 14 days in the presence of 400 μg/ml G418 (for YFP:TLR4) and 200 μg/ml hygromycin B (for MD2 and CD14). Candidate colonies were selected based on YFP fluorescence and cloned by limiting dilution.

Prior to TIRF imaging, HEK-293/MD2/CD14/YFP:TLR4 cells were harvested using a non-enzymatic cell dissociation reagent (Cell Stripper, Mediatech) to avoid proteolytic damage to cell surface receptors that may occur if trypsin is used. Cells were then incubated with 100nM Alexa Fluor 647-labeled LPS of the indicated type for 15 minutes, pelleted by centrifugation, and washed with medium. Resuspended cells in medium were then added to coverslip-bottom dishes on the microscope stage pre-equilibrated to 37°C in a microincubator above the heated objective. TIRF images were collected and analyzed as described above. Figure 21 shows preliminary images obtained just before the project ended. Although no differences in TLR4/LPS cluster size or intensity were apparent, we believe subsequent experiments varying the concentration of LPS, staining time, and host cell type will be necessary to definitively analyze this interaction.

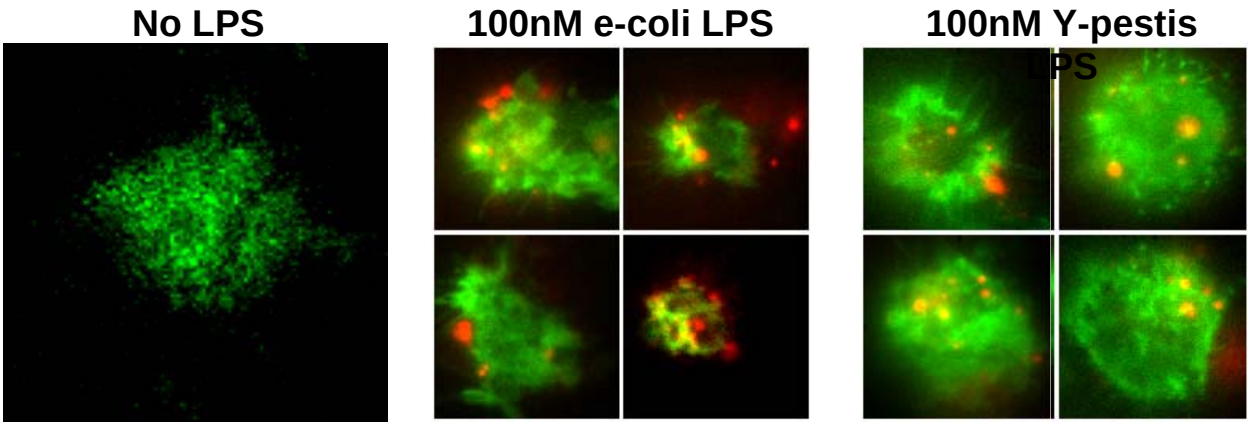

Figure 21: Dual color TIRF images of E. coli or Y. pestis LPS bound to transfected HEK-293 cells. Note aggregation of TLR4/LPS complexes in the plasma membrane.

5. MOLECULAR DYNAMICS OF PROTEINS IN LIPID BILAYER

We have performed simulations that help understand deviations from the standard Saffman-Delbruck diffusion of proteins in a lipid bilayer. Recent experiments (Gambin et al., 2006) have found that the scaling of the diffusion as a function of the protein radius R can have a $1/R$ dependence in addition to the standard log R dependence. Theoretical work by Naji, and colleagues (Naji et al., 2007) calculated corrections to Saffman-Delbruck that yield the 1/R dependence. These calculations treat the continuum hydrodynamics, but do not include the molecular scale phenomena. One interpretation is that the attraction between the lipids and the protein form a 'cloud' of lipids around the protein that move with the protein and alter the dependence. They have an alternative interpretation in which the water near the protein has the same behavior. We have examined both the experimental and theoretical works with our coarse-grained simulations.

We use a coarse-grained bead-spring model for the lipids and water. The model distinguished between the head and tail groups via simple Lennard-Jones (LJ) interactions. The head group beads ‘like’ the water and other head group beads; these interactions are attractive. The tail group beads do not ‘like’ the water or the head group beads and have repulsive interactions with them. The interactions between tail group beads are attractive. With these interactions random initial configurations of lipids and water will self-assembly into lipid bilayers. The liquid dynamics of the lipid bilayer is readily apparent. The major advantage of the coarse-grained models is the ability to reach time scales for which lipid diffusion can be easily measured. To introduce proteins in the model, we have treated alpha helices. Each residue is treated as a single bead. The helical structure is maintained by a dihedral position and an extra bond between every 4th residue, which represents the hydrogen bonding that forms the alpha helix. The hydrophobic and hydrophilic residues are treated in the same manner as the corresponding groups in the lipid. We have constructed transmembrane alpha helices that have hydrophilic ends and a hydrophobic middle. The results below are for helices that have lengths that match the lipid bilayer.

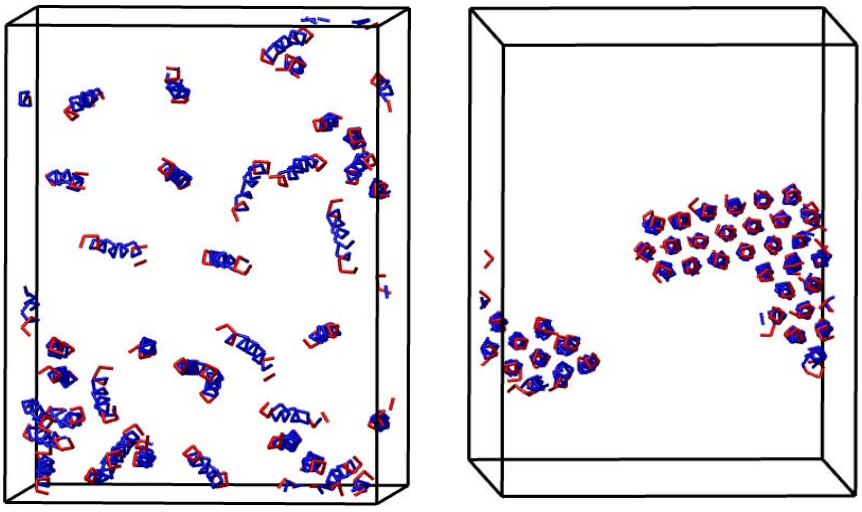

Figure 22: An aggregate of helices forms (right) starting from a random configuration (left) of 40 alpha helices in a lipid bilayer (not shown).

The main difficulty in calculating the diffusion of a single alpha helix in the bilayer is the poor statistics due to having only a single helix. To improve statistics, we performed simulations at different concentrations of the alpha helices. In the limit of zero concentration, we would obtain the single helix diffusion constant. In addition, the simulations with many helices directly study the effect of (many) obstacles on the diffusion of the helices. With the interactions as described above we studied systems with varying number of alpha helices. However, we found that the alpha helices aggregate into clusters (Figure 22). This result was unexpected given that the interaction between helices, between lipids and between lipids and helices are all the same. The lipids are in the liquid phase. The total interaction between helices should be about the same as the interaction between lipids. One main difference is that the helices span the full bilayer, but that in itself will not result in aggregation. The total LJ interaction between a pair of helices is equal to the interaction among 4 lipids (2 on each leaflet). Thus the entropy of the lipids will be larger. In addition, the helices are stiffer, which reduces their entropy. Thus, there should be a greater propensity for aggregation of the helices relative to the lipids, but at this interaction strength aggregation was not expected. This result is very interesting with respect to studying the formation of clusters of alpha helix, for example in antimicrobial peptides. We have shown that aggregation can be simulated using these models.

In order to obtain diffusion data aggregation must be suppressed. For this reason, the interaction between beads on two alpha helices was set to be purely repulsive, which just provides the excluded volume interaction. The interaction between lipid and helix remained the same as before. As expected, no aggregation occurred using this parametrization and in the limit of low concentration there is no difference between this case and one with attractive interactions between helices, since in the single helix limit there are no helix:helix interactions. For a base system of 440 lipids without helices, simulations have been performed with 10, 20, 30 and 40 helices. Figure 23 shows the mean squared displacement as a function of time. The slope of the data gives the diffusion constant. Least squares fits give 1.23, 1.13, 1.17, 1.18 • 10^{-3} in LJ units. Within the uncertainty of the data, little or no dependence on the number of helices occurs for these simulations with the interactions between helices turned off. Pursuant to confirmation by simulations of larger systems that there is no system size effect, we can now calculate the diffusion of proteins and by making coupled alpha helices, simulations of protein diffusion as a function of protein radius can be done.

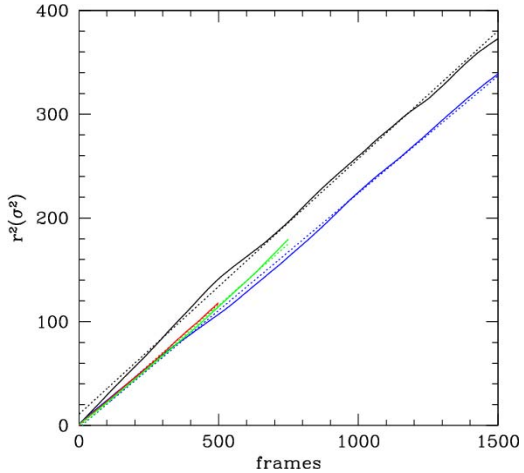

Figure 23: Plot of mean squared displacement as a function of the simulation frames (10000 time steps) for 10 (black), 20(blue), 30 (red) and 40 (green)

6. CONCLUSIONS

This project has been a successful demonstration of multidisciplinary teamwork and collaboration across departments and between institutions (UNM & Sandia National Laboratories). We have met or exceeded all of our technical milestones and achieved our ultimate goal of increasing our fundamental knowledge of the spatial-temporal relationships of receptors and their associated signaling proteins and lipids during the very early events in cellular signal transduction. The TIRF microscope has been an enabling technology for a variety of projects including collaborations in cell signaling, cell sensors, and JBEI related lignocellulose deconstruction. Our presentation and publication record includes 11 presentations, 2 invited presentations, one conference proceedings, as well as one publication already in print, another submitted, and a third to be submitted by the end of the fiscal year. Two additional peer-reviewed publications are anticipated to be submitted shortly. (Publications and presentation are detailed in Appendix A.) Our accomplishments have led to the submission of multiple proposals in the area of cellular signaling both Sandia-led and teaming with other institutions, including our collaborative efforts in the recently funded New Mexico Spatial Temporal Modeling Center (STMC) which should open doors for greater UNM/SNL/LANL collaboration.

4. REFERENCES

Andrews, N. L., Lidke, K. A., Pfeiffer, J., Burns, A. R., Wilson, B. S., Oliver, J. M., and Lidke, D. (2008a). *Nature Cell Biology* **10,** 955

Andrews, N. L., Lidke, K. A., Pfeiffer, J. R., Burns, A. R., Wilson, B. S., Oliver, J. M., and Lidke, D. S. (2008b). *Nat Cell Biol* **10,** 955.

Axelrod, D. (2001). *Traffic* **2,** 764.

Axelrod, D., Burghardt, T. P., and Thompson, N. L. (1984). *Annu Rev Biophys Bioeng* **13,** 247.

Carpenter, S., and O'Neill, L. A. (2009). *Biochem J* **422,** 1.

Carroll-Portillo, A., Spendier, K., Lidke, K., Pfeiffer, J., Lidke, D., Thomas, J., Wilson, B., and Timlin, J. A. (2009). *Journal of Immunology***,** submitted.

Chesla, S. E., Selvaraj, P., and Zhu, C. (1998). *Biophysical Journal* **75,** 1553.

Darveau, R. P., and Hancock, R. E. (1983). *J Bacteriol* **155,** 831.

Davey, A. M., Walvick, R. P., Liu, Y., Heikal, A. A., and Sheets, E. D. (2007). *Biophys J* **92,** 343.

Digman, M. A., Dalal, R., Horwitz, A. F., and Gratton, E. (2008). *Biophys J* **94,** 2320.

Dustin, M. L. (2008). *Adv Exp Med Biol* **640,** 164.

Flad, H. D., Loppnow, H., Rietschel, E. T., and Ulmer, A. J. (1993). *Immunobiology* **187,** 303.

Fomsgaard, A., Freudenberg, M. A., and Galanos, C. (1990). *J Clin Microbiol* **28,** 2627.

Gambin, Y., Lopez-Esparza, R., Reffay, M., Sierecki, E., Gov, N. S., Genest, M., Hodges, R. S., and Urbach, W. (2006). *Proceedings of the National Academy of Sciences of the United States of America* **103,** 2098.

Geha, R. S., Jabara, H. H., and Brodeur, S. R. (2003). *Nat Rev Immunol* **3,** 721.

Hamawy, M. M., Oliver, C., and Siraganian, R. P. (1992). *J Immunol* **148,** 524.

Holowka, D., Gosse, J. A., Hammond, A. T., Han, X., Sengupta, P., Smith, N. L., Wagenknecht-Wiesner, A., Wu, M., Young, R. M., and Baird, B. (2005). *Biochim Biophys Acta* **1746,** 252.

Karkhanis, Y. D., Zeltner, J. Y., Jackson, J. J., and Carlo, D. J. (1978). *Anal Biochem* **85,** 595.

Kinet, J. P. (1999). *Annu Rev Immunol* **17,** 931.

Larson, D. R., Gosse, J. A., Holowka, D. A., Baird, B. A., and Webb, W. W. (2005). *J. Cell Biol.* **171,** 527.

Ma, Z., Sharp, K. A., Janmey, P. A., and Finkel, T. H. (2008). *PLoS Biology* **6,** e43.

Miller, S. I., Ernst, R. K., and Bader, M. W. (2005). *Nat Rev Microbiol* **3,** 36.

Montminy, S. W., Khan, N., McGrath, S., Walkowicz, M. J., Sharp, F., Conlon, J. E., Fukase, K., Kusumoto, S., Sweet, C., Miyake, K., Akira, S., Cotter, R. J., Goguen, J. D., and Lien, E. (2006). *Nat Immunol* **7,** 1066.

Naji, A., Levine, A. J., and Pincus, P. A. (2007). *Biophys J* **93,** L49.

Perrigoue, J. G., Saenz, S. A., Siracusa, M. C., Allenspach, E. J., Taylor, B. C., Giacomin, P. R., Nair, M. G., Du, Y., Zaph, C., van Rooijen, N., Comeau, M. R., Pearce, E. J., Laufer, T. M., and Artis, D. (2009). *Nat Immunol* **10,** 697.

Petersen, N. O., Hoddelius, P. L., Wiseman, P. W., Seger, O., and Magnusson, K. E. (1993). *Biophys J* **65,** 1135.

Pierce, S. K. (2002). *Nat Rev Immunol* **2,** 96.

Rebeil, R., Ernst, R. K., Gowen, B. B., Miller, S. I., and Hinnebusch, B. J. (2004). *Mol Microbiol* **52,** 1363.

Robbins, M. S., and Hadwen, B. J. (2003). *IEEE Transactions on Electron Devices* **50,** 1227.

Sato, S. B., Ishii, K., Makino, A., Iwabuchi, K., Yamaji-Hasegawa, A., Senoh, Y., Nagaoka, I., Sakuraba, H., and Kobayashi, T. (2004). *J Biol Chem* **279,** 23790.
Smith, A. J., Pfeiffer, J. R., Zhang, J., Martinez, A. M., Griffiths, G. M., and Wilson, B. S. (2003). *Traffic* **4,** 302.
Sohn, H., Tolar, P., and Pierce, S. (2008). *The Journal of Cell Biology* **182,** 367.
Sokol, C. L., Chu, N. Q., Yu, S., Nish, S. A., Laufer, T. M., and Medzhitov, R. (2009). *Nat Immunol* **10,** 713.
Surviladze, Z., Harrison, K. A., Murphy, R. C., and Wilson, B. S. (2007). *J Lipid Res* **48,** 1325.
Tolar, P., Sohn, H. W., and Pierce, S. K. (2008). *Immunol Rev* **221,** 64.
Triantafilou, K., Triantafilou, M., and Fernandez, N. (2000). *Cytometry* **41,** 316.
Unruh, J. R., and Gratton, E. (2008). *Biophys J* **95,** 5385.
Visintin, A., Mazzoni, A., Spitzer, J. A., and Segal, D. M. (2001). *Proc Natl Acad Sci U S A* **98,** 12156.
Wilson, B. S., Pfeiffer, J. R., Surviladze, Z., Gaudet, E. A., and Oliver, J. M. (2001). *J Cell Biol* **154,** 645.
Wilson, B. S., Steinberg, S. L., Liederman, K., Pfeiffer, J. R., Surviladze, Z., Zhang, J., Samelson, L. E., Yang, L. H., Kotula, P. G., and Oliver, J. M. (2004). *Mol Biol Cell* **15,** 2580.
Wiseman, P. W., and Petersen, N. O. (1999). *Biophys J* **76,** 963.
Yoshimoto, T., Yasuda, K., Tanaka, H., Nakahira, M., Imai, Y., Fujimori, Y., and Nakanishi, K. (2009). *Nat Immunol* **10,** 706.
Young, R. M., Holowka, D., and Baird, B. (2003). *J Biol Chem* **278,** 20746.

APPENDIX A: SUMMARY OF PRESENTATIONS AND PUBLICATIONS

Below is a list of presentations and publications that were enabled with full or partial funding from this LDRD project.

Presentations:

J. A. Timlin, A. Carroll-Portillo, K. Spendier, J. Aaron, J. Pfeiffer, K. Lidke, D. Lidke, J. Thomas & B. Wilson, "Imaging of IgE Receptor Dynamics at the Mast Cell Synapse", presented at *World Molecular Imaging Congress*, Montreal, Canada, **September 22 - 26**, **2009**. *(poster)*

K. Spendier, A. Carroll-Portillo, K. Lidke, B. Wilson, J. A. Timlin & J. L. Thomas, "Redistribution of Mast Cell IgE receptors in contact with Membrane-Bound Haptens", presented at *2009 CINT Users Conference*, Santa Fe, NM, **September 28-29, 2009**. *(poster)*

A. Carroll-Portillo, K. Spendier, K. Lidke, J. Pfeiffer, D. Lidke, J. Thomas, J. A. Timlin & B. Wilson, "High Resolution Imaging of FcεRI at the Mast Cell Synapse ", presented at *Immunity 2009*, Seattle, WA, **May 8-12, 2009**. *(poster)*

J. Aaron, A. Carroll-Portillo, J. Pfeiffer, B. Wilson & J. A. Timlin, "Imaging Adaptive Immune Response in Single Cells using TIRF Microscopy", presented at *Microscopy & Microanalysis*, Richmond, VA, **Jully 26 - July 30**, **2009**. *(presentation)*

K. Spendier, A. Carroll-Portillo, K. Lidke, B. Wilson, J. A. Timlin & J. Thomas, "Mobile Haptens in Lipid Bilayers Cause Large-Scale Clustering of IgE Receptors ", presented at *Biophysical Society Annual Meeting*, Boston, MA, **February 28 - March 4**, **2009**. *(poster)*

J. Aaron, A. Carroll-Portillo, J. Pfeiffer, B. Wilson & J. A. Timlin, "TIRF Microscopy for Imaging Acquired Immune Responses", presented at *Bioscience & Technology Forum*, Albuquerque, NM, **January 26 - 27**, **2009**. *(poster)*

J. A. Timlin, A. Carroll-Portillo, J. Pfeiffer, H. Li, G. Griffiths, J. Oliver & B. Wilson, "Visualizing cholesterol dynamics in the living cell membrane", presented at *FACSS*, Reno, NV, **September 28 - October 2**, **2008**. *(invited presentation)*

A. Carroll-Portillo, R. M. Noek, B. Carson, R. Rebeil & J. A. Timlin, "Spatial and Temporal Interactions of TLR4 Pathway Membrane Components Revealed by Total Internal Reflection Fluorescence (TIRF) Microscopy", presented at *Microscopy & Microanalysis*, Albuquerque, NM, **August 3-7**, **2008**. *(presentation)*

A. Carroll-Portillo, R. M. Noek, K. Lidke, J. Pfeiffer, B. Wilson, J. Oliver, A. Burns & J. A. Timlin, "Ligand presentation for fluorescent visualization of receptor membrane dynamics using Total Internal Reflection Fluorescence (TIRF) microscopy", presented at *In Vitro Imaging*, San Diego, CA, **November 27-28**, **2007**. *(poster)*

K. Lidke, N. Andrews, D. Lidke, J. Pfeiffer, J. Oliver, B. Wilson & A. Burns, "Direct observation of confined motion of membrane proteins associated with actin corrals", presented at *Biophysical Society Annual Meeting*, Baltimore, MD, **March 3 - March 7**, **2007**. *(poster)*

N. Andrews, K. Lidke, D. Lidke & A. Burns, "FceRI diffusional dynamics measured by single quantum dot tracking in resting and activated cells", presented at *Biophysical Society Annula Meeting*, Baltimore, MD, **March 3 - March 7**, **2007**. *(poster)*

Conference Proceedings:

D. S. Lidke, N. L. Andrews, J. R. Pfeiffer, H. D. T. Jones, M. B. Sinclair, D. M. Haaland, A. R. Burns, B. S. Wilson, J. M. Oliver & K. A. Lidke, "Exploring membrane protein dynamics by multicolor single quantum dot imaging using wide field, TIRF, and hyperspectral microscopy", in *Colloidal Quantum Dots for Biomedical Applications II,* San Jose, CA, **2007**.

Peer-Reviewed Publications:

N. L. Andrews, K. A. Lidke, J. Pfeiffer, A. R. Burns, B. S. Wilson, J. M. Oliver & D. Lidke, "Actin restricts FcεRI diffusion and facilitates antigen-induced receptor immobilization", *Nature Cell Biology,* 10**,** 955 - 963, **2008**.

A. Carroll-Portillo, K. Spendier, K. Lidke, J. Pfeiffer, K. Lidke D. Lidke, J. Thomas, B. Wilson & J. A. Timlin, "Formation of a Mast Cell Synapse: FcεRI Membrane Dynamics upon Binding Mobile or Immobilized Ligands on Surfaces," *Journal of Immunology,* submitted, **2009**.

K. Spendier, A. Carroll-Portillo, K. A. Lidke, B. S. Wilson, J. A. Timlin, J. Thomas " Distribution and dynamics of RBL IgE receptors (FcεRI) observed on planar ligand-presenting surfaces ", *Biophysical Journal,* in preparation, **2009**.

J. Aaron, B. Wilson, J. Timlin, “Monitoring Degranulation in Live Mast Cells at the Single Cell Level”, *Microscopy and Microanalysis,* in preparation, **2009**.

DISTRIBUTION

3 University of New Mexico, Department of Pathology
Attn: Bridget Wilson (1)
Attn: Amanda Carroll-Portillo (1)
Attn: Janet Oliver (1)
University of New Mexico,
Albuquerque, New Mexico 87131

3 University of New Mexico, Department of Physics and Astronomy
Attn: James Thomas (1)
Attn: Kathin Spendier (1)
Attn: Keith Lidke (1)
University of New Mexico
Albuquerque, New Mexico 87131

1	MS0351	Alan Burns	01012
1	MS0895	Jerilyn Timlin	08622
1	MS1315	Mark Stevens	01814
1	MS1413	Bryan Carson	08622
1	MS1413	Jesse Aaron	08622

1	MS0899	Technical Library	9536 (electronic copy)
1	MS0123	D. Chavez, LDRD Office	1011


Sandia National Laboratories